International Journal of Impact Engineering 167 (2022) 104261

Contents lists available at ScienceDirect

International Journal of Impact Engineering

journal homepage: www.elsevier.com/locate/ijimpeng

Aluminium plates with geometrical defects subjected to low-velocity impact: Experiments and simulations

Vetle Espeseth [*,a], Tore Børvik [a,b], Odd Sture Hopperstad [a,b]

[a] Structural Impact Laboratory (SIMLab), Department of Structural Engineering, NTNU, Norwegian University of Science and Technology, Trondheim NO-7491, Norway
[b] Centre for Advanced Structural Analysis (SFI CASA), NTNU, Trondheim, Norway

ARTICLE INFO

Keywords:
Drop tower tests
AA6016
Crack propagation
Ductile tearing
Experimental validation
Finite element analysis

ABSTRACT

In this paper, an experimental and numerical program investigating impact in the low-velocity regime ($\leq$ 10 m/s) on 1.5 mm thick AA6016 aluminium plates in three different heat treatments (T4/T6/T7) is presented. The tests were carried out in a drop tower where the force was continuously monitored by a strain-gauge instrumented striker. Results from both intact plates and plates with geometrical defects in the form of pre-cut slits are presented. The heat treatments result in materials with different strength, work-hardening and ductility. It was observed that the intact plates in high-strength material are more resilient to low-velocity impact whereas high ductility is preferred for the plates with pre-cut slits as the crack growth is more restrained. Quasi-static tests on the same plates showed a significant reduction in force only for plates in temper T6 and T7. The experiments are complemented by nonlinear finite element simulations using linear brick elements in Abaqus/Explicit. A von Mises plasticity model was calibrated from notched tension tests. The global response from single edge notch tension (SENT) tests was used to calibrate the failure criterion. The numerical model was able to sufficiently predict the force response and deformation of the intact plates, and the global response and crack propagation of the SENT tests. While the force response in the dynamic simulation of low-velocity impact on plates with slits was in agreement with the observed quasi-static response for all tempers, it was in general underestimated for temper T6 and T7 when compared to the data from the dynamic experiments. For plates in temper T4, the predicted response also agreed with the dynamic experiments.

1. Introduction

The use of thin-plate structures of steel or aluminium alloys is widespread in engineering applications, such as in the automotive, marine and aviation industries. These plated structures are highly sensitive to crack formation and growth which can substantially reduce their performance and integrity during e.g. impact loading. The ability to predict material failure can therefore be a crucial factor in the design of such structures.

The literature on thin metal plates (without initial geometrical defects) subjected to impact loading is considerable. A majority of these studies consider ordnance and sub-ordnance velocity projectiles where the research aims to find or predict the ballistic limit velocity of the target plate (see e.g. the review of Corbett et al. [1]). Low-velocity impact events, where the impacting body has a velocity usually less than 50 m/s, includes dropped objects, vehicle impacts and ship collisions. Early work covering such events are reported by, among others, Langseth and Larsen [2–4], Wen and Jones [5,6] and Langseth et al. [7]. A common conclusion in these and other studies concerning low-velocity impact events on ductile plates, where the impacting mass is significantly larger than the mass of the target plates, is that the inertia effects are practically negligible. Consequently, a quasi-static method of analysis is expected to be sufficient, provided that the material exhibits low rate sensitivity. Grytten et al. [8] considered low-velocity perforation of AA5083-H116 aluminium plates that were clamped in a circular frame and struck by a blunt-nosed projectile. Grytten et al. [9] and Fagerholt et al. [10] performed a quasi-static and low-velocity impact study, respectively, on the same material and geometry with the emphasis on continuously monitoring the out-of-plane deformation using structured light and close-range photogrammetry. Holmen et al. [11] performed experiments and numerical simulations of impact by blunt- and ogival-ended impactors on multi-layered dual-phase steel plates to investigate the perforation resistance. A 3D digital image correlation technique was used to continuously measure the out-of-plane

* Corresponding author.
E-mail address: vetle.espeseth@ntnu.no (V. Espeseth).

https://doi.org/10.1016/j.ijimpeng.2022.104261
Received 15 December 2021; Received in revised form 28 February 2022; Accepted 30 April 2022
Available online 5 May 2022

displacement field of the plates. Gruben et al. [12] conducted an experimental and numerical study of quasi-static and low-velocity impact on high-strength steel plates with different geometries. The plates failed under pre-dominant membrane loading. The stress state prior to failure ranged from uniaxial tension to equi-biaxial tension, depending on the specimen geometry, covering the most important stress states that occur during an impact event on a thin-walled structure.

The research on the dynamic response of plates with geometrical defects is more scarce. Such defects have for instance been introduced when investigating the combined effects of fragment impact and blast pressure [13–17]. Only a modest reduction in the structural resistance was observed for plates with defects when the impulse was sufficiently low. For higher loads, crack initiation and propagation occurred at the geometrical defects, which resulted in early structural collapse. Granum et al. [15] investigated the effects of pre-cut slits on the dynamic response of AA6016 aluminium alloy plates subjected to pressure loads. The effects of strength, work-hardening and ductility were investigated by considering different heat-treatments. It was found that high ductility rather than high strength is favourable for plates with pre-cut slits as crack growth was reduced under blast loading. A similar finding was reported by Elveli et al. [14] when comparing blast resistance of dual-phase, medium-strength, high-hardening steel to martensitic, high-strength, low-hardening steel.

It can be challenging to apply the correct loads in simulations of blast problems without accounting for fluid-structure interactions, especially for high blast intensities [18]. Moreover, the numerical results in these studies have mainly been verified against the experimental data by visual comparison and measurements of the displacement of the deformed profile, while there is no direct comparison of the total force exerted on the plate. Experiments on dynamic crack growth in plates subjected to impact loading can therefore be useful in the validation of numerical models as the load case is less complex and can be accurately modelled using the finite element method. Moreover, the resisting force between the impacting body and the plate can readily be measured during impact.

A considerable amount of research has been done on ductile tearing of metal plates. The governing mechanisms of ductile tearing are the nucleation of micro-voids at intermetallic inclusions that subsequently grow during plastic straining and eventually coalesce to form micro-cracks and subsequently macro-cracks, resulting in material separation [19]. Cup-cup, cup-cone and slant fracture are the three different failure modes that are observed in tear tests of plates, and they often occur in combination. While slant fracture is mainly observed for high-strength aluminium alloys [20,21], cup-cup fracture is more common for plates made of a low-strength material [22].

It is, however, not fully resolved why one failure mode is preferred over the other. El-Naaman and Nielsen [23] studied tearing of a normal strength steel and a softer AA1050 aluminium alloy under global mode I loading with the emphasis on the different failure modes. They suggested that the interplay between the initial porosity, the rate of void nucleation and growth, and the necking process determines whether cup-cup or slant fracture occurs. Experimental evidence indicates that cup-cup fracture is favoured where extensive void growth and thus thinning of the process zone occur. As the rolling direction of the plate was found to influence the fracture surface morphology, it was suggested that the orientation of the grains and anisotropy within the material also influence the fracture mode. Simonsen and Törnqvist [24] reported a slanted crack that systematically flipped back and forth in their experimental study of ductile crack propagation in edge crack and centre crack plate specimens. This flipping of the slanted fracture surface has also been studied in El-Naaman and Nielsen [23], Felter and Nielsen [25], Nielsen and Gundlach [26] and Nielsen and Felter [27].

The stress state is recognized as one of the prime factors that influence the fracture strain of a given material subjected to plastic deformation. While the effect of the stress triaxiality is well established [28,29], recent studies address the role of the deviatoric stress state on the damage evolution in ductile materials [30,31,32]. The credibility of different fracture models for steel and aluminium alloys has been addressed in Gruben et al. [33], Li et al. [34], Wierzbicki et al. [32] and Lian et al. [35], where predictions are compared with data obtained from tests on various specimen types. While more sophisticated fracture models often show good performance over a large range of stress states, the number of mechanical tests needed and the added complexity in the calibration procedure make such models inappropriate for many industrial applications [32]. As a remedy, Morin et al. [36] and Granum et al. [37] proposed a hybrid experimental-numerical approach that utilizes localization analyses to generate failure loci, which proved to be a cost-effective and versatile tool for reducing the number of mechanical tests required to calibrate advanced fracture models. On the other hand, the simple one-parameter fracture model by Cockcroft and Latham [38] has been used successfully in several applications, see e.g. Dey et al. [39], Kane et al. [40], Lian et al. [35] and Costas et al. [41], and is often favoured for its simplicity and versatility. However, the dependency on stress triaxiality and deviatoric stress state is only implicitly accounted for in the Cockcroft–Latham fracture model and care must be taken when this model is used for structures where failure can occur within a wide range of stress states.

In this study, the response of AA6016 aluminium plates with different heat-treatments subjected to low-velocity impact loading of different intensities is investigated experimentally and numerically. The study includes plates with geometrical defects in the form of pre-cut slits in the centre as well as plates without any geometrical defects. The plates are heat-treated to temper T4, T6 and T7 with different strength, work-hardening capacity and ductility. The overall goal of the study is twofold: to evaluate the effect of the geometrical defects on the response of the plates with different heat treatments, and to assess the credibility of a finite element based simulation model, where von Mises plasticity is combined with the Cockcroft–Latham fracture model, in predicting the observed behaviour of the plates. Material tests on dog-bone and notched specimens are performed to quantify the material properties. A single edge notch tension (SENT) type of test is used to investigate ductile tearing under simple quasi-static conditions. A dropped-object-rig is used to perform the low-velocity impact test, where the plates are struck by an impactor with a large hemispherical nose. The resisting force between the nose and the plate is measured during impact and synchronized high-speed cameras are used for visual comparison and digital image correlation (DIC) measurements. The response of the plates from the impact tests are compared to quasi-static push-through tests on plates with the same geometry and boundary conditions. Explicit finite-element simulations of the quasi-static material tests and the low-velocity impact tests are performed in Abaqus/Explicit using solid elements. The tensile tests on notched specimens are used to calibrate the yield stress and work-hardening of the material, the SENT tests are used in the calibration of the Cockcroft–Latham fracture model, and the impact tests and quasi-static push-through tests are used for assessment of the modelling approach. Element erosion is used to represent the formation and propagation of cracks in the finite element simulations. To evaluate the results, the stress state in the elements along the crack is analyzed and a parametric study on the influence of rate dependence, friction, failure model and thermal softening of the material due to adiabatic heating is presented.

2. Material characterization

2.1. Materials

The AA6016 aluminium plates tested in the experimental study were provided by Hydro Aluminium Rolled Products in Bonn in the three different tempers T4, T6 and T7. Due to its high strength, good formability and surface quality, this particular alloy is mainly used as outer body panels in the automotive industry. To obtain temper T4, the plates

were solution heat-treated at 530 °C, then air quenched, pre-baked at 80 °C and finally naturally aged to a stable condition. Temper T6 and T7 were obtained by artificial ageing plates of temper T4 for 5 h at 185 °C and 24 h at 205 °C, respectively. Plates of the same materials have previously been characterized by Granum et al. [15,37] and we refer to these two studies for the chemical composition of the alloy and additional mechanical tests, including plane-strain tension and simple shear tests. The plates used in this work show a slightly different mechanical response as they originate from a different batch. We will therefore report on some mechanical tests in this section. In addition, single edge notch tension tests were performed to investigate the fracture process initiated by a sharp geometrical imperfection under quasi-static loading conditions. The mean thickness of the plates was found to be 1.497 mm with a standard deviation of 0.014 mm. A thickness of 1.5 mm is therefore assumed for the most part of this study as the small variation was found to be insignificant. All specimens were extracted from the aluminium plates using wire erosion.

2.2. Uniaxial tension tests

Uniaxial tension tests on dog-bone specimens were performed to determine common material properties and give a first estimate of the hardening behaviour of the different tempers. The initial width and length of the gauge section of the specimens were 12.5 mm and 70 mm, respectively, and a sketch of the geometry can be found in Granum et al. [37]. To disclose any effects of anisotropy, specimens with an orientation of 0°, 45° and 90° with respect to the rolling direction were considered. All tests were carried out in an Instron 5985 series universal testing machine where the force was measured by a 100 kN load cell attached to the actuator. A constant cross-head velocity of 2.1 mm/min was used, resulting in an initial strain rate of 5×10^{-4} s^{-1} in the gauge region before the occurrence of necking. The tests were monitored using a Basler acA4112-30 um camera with a Samyang 100 mm f/2.8 ED UMC macro lens at a frame rate of 1 Hz. The strain field on the surface of the specimen was obtained from 2D digital image correlation (2D-DIC), using the in-house software eCorr [42]. A spray-painted speckle pattern was applied onto the surface of the specimen to allow for better tracking of the local displacement. The elongation in the gauge region was found from a virtual extensometer with an initial length of 50 mm.

The engineering stress-strain curves are shown in Fig. 1 for all tensile directions and tempers. A total of four repeated tests were performed for each direction. The load level is similar in the repeated tests, but the elongation at which the stress starts to drop shows some variation. Only the test with the response closest to the average within a given direction is included in Fig. 1 to emphasize the influence of tensile direction. The similarity in flow stress in the three directions suggests that the material exhibits close to isotropic properties with respect to strength and strain hardening. Granum et al. [15] reported Lankford coefficients R less than unity for all tempers, indicating a material that is prone to thinning and exhibits a moderate anisotropy in plastic flow. The Lankford coefficient is somewhat higher in the rolling direction than in the two other directions for all tempers.

The 0.2% proof stress, ultimate tensile strength and logarithmic strain at necking are compiled in Table 1 for specimens in the 0° direction. Temper T6 displays the highest proof stress and tensile strength. The proof stress of temper T7 is slightly higher than for temper T4, while temper T4 exhibits a stronger work hardening and higher tensile strength than temper T7. The logarithmic strain at necking is the highest for temper T4, followed by T6 and T7.

The local equivalent strain fields in the necked region of the specimens at failure are shown on the right side of Fig. 1 for one specimen of each temper loaded in the 0° direction. The equivalent strain is defined by $\varepsilon_{\text{eq}} = \sqrt{\frac{4}{3}(\varepsilon_1^2 + \varepsilon_1\varepsilon_2 + \varepsilon_2^2)}$, where ε_1 and ε_2 are the principal logarithmic strains. An element size of approximately 1 mm was used in the 2D-DIC analyses. The failure strain is taken as the equivalent strain of the critical element, i.e., the element with the highest strain, and the average value from all repeated tests in the 0° direction is summarized in Table 1. The procedure follows the method described in Qvale et al. [43]. These values represent the strain at the surface of the specimen at failure, but should not be interpreted as an absolute measure of the failure strain as the resolution of the measurements is not high enough to capture the maximum local strain. However, the failure strain can be compared between different tempers as the element size is identical. Thus, T7 is the most ductile temper with the highest failure strain, followed by temper T4, while temper T6 has the lowest ductility. The higher failure strain of temper T7 is also featured in the stress-strain curves of Fig. 1 as the large drop in stress level at the tail of the

Table 1
0.2% proof stress, ultimate tensile strength, logarithmic strain at necking and failure strain in the necked region for the specimens in the rolling direction. The measurements are taken as the average between all test specimens within this orientation, and the difference between the average value and the upper and lower values is specified in the sub- and superscript.

Temper	0.2% proof stress [MPa]	Ultimate tensile strength [MPa]	Log. strain at necking [–]	Failure strain from 2D-DIC [–]
T4	$133.6^{+0.8}_{-0.8}$	$248.2^{+0.2}_{-0.2}$	$0.223^{+0.002}_{-0.001}$	$0.591^{+0.013}_{-0.013}$
T6	$237.2^{+0.8}_{-1.0}$	$280.7^{+0.9}_{-0.5}$	$0.104^{+0.003}_{-0.002}$	$0.329^{+0.010}_{-0.019}$
T7	$151.4^{+0.2}_{-0.2}$	$194.3^{+0.5}_{-0.8}$	$0.071^{+0.002}_{-0.002}$	$0.720^{+0.014}_{-0.020}$

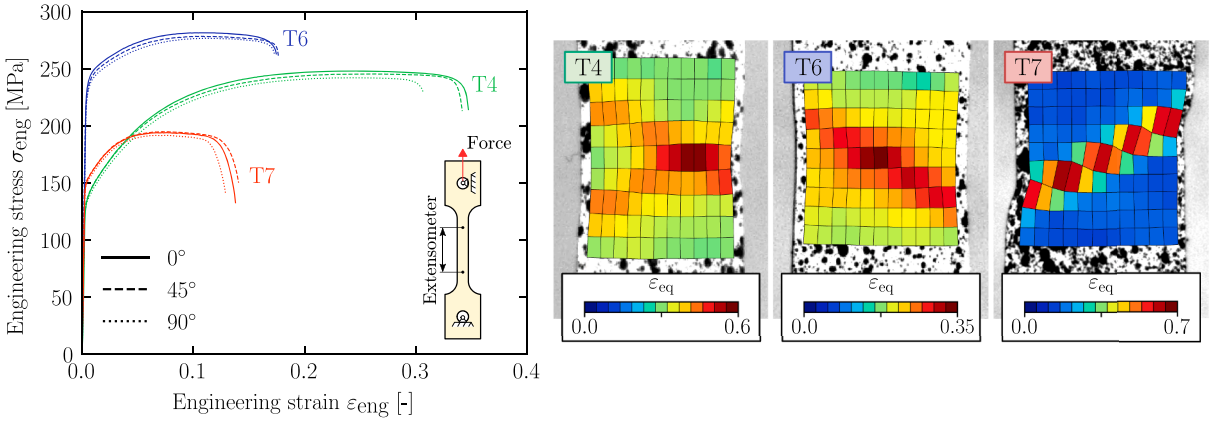

Fig. 1. Engineering stress-strain response (left figure) and the local equivalent strain field at the surface in the necked region just before specimen failure (right figures). The different tempers are defined by different colours, while the line style indicates the direction of the specimen with respect to the rolling direction. The strain fields at the surface are calculated using 2D-DIC on the 0° direction specimens with an element size of approximately 1 mm.

curves. We notice from the strain fields in Fig. 1 that the strain outside of the necked region is, in general, higher for temper T4 as the strain at necking is much larger for this temper than for temper T7.

2.3. Notch tension tests

Notch tension tests were used in this work to calibrate the isotropic hardening rule of the von Mises plasticity model applied in the finite element simulations. The notch introduces a strain concentration that predetermines the location of the neck and the symmetry is preserved in the post-necking range [44,45]. Compared to the straight dog-bone specimens, these tests show excellent repeatably also after the maximum force is reached, making them well suited for calibration of the isotropic hardening rule at large strains. The notch radius of the specimens denoted NT3 and NT10 is 3.35 and 10 mm, respectively. The minimum width of the gauge area over the notch is 5 mm for both specimen types. We refer to Granum et al. [37] for a detailed sketch of the specimen geometries. Only specimens loaded in the rolling direction (0° direction) were tested. A spray-painted speckle pattern was applied onto the surface of the specimens to allow for full-field measurements of the surface strain (2D-DIC). The tests were carried out in an Instron 5566 series universal testing machine where the force was measured by a 10 kN load cell attached to the actuator. A constant cross-head velocity of 0.6 mm/min was used in all tests. The tests were monitored using a Basler acA2440-75 um camera with a Samyang 100 mm f/2.8 ED UMC macro lens at a frame rate of 4 Hz. Similar to the dog-bone tests, a virtual extensometer in eCorr with an initial length of 15 mm was used to monitor the global elongation over the notch. A local virtual extensometer with an initial length of 2 mm, placed centric to the notch radius, was used to measure the logarithmic strain inside the notched region.

The force and the local logarithmic strain as a function of the global elongation are shown in Fig. 2 for both specimens types. Three repeated tests were carried out for each specimen and temper. We have here only included one of the repeated tests in the figure due to the excellent repeatability. The force level obtained with the two specimen types is comparable while the NT10 specimen exhibits a somewhat larger elongation before failure. As for the tests on the dog-bone specimens, the maximum load is obtained at a substantially higher elongation for temper T4 than for temper T6 and T7. The local strain at failure is lower for the specimen with the sharpest notch. The sharper notch results in a slightly higher stress triaxiality inside the necked region (see Fig. 14), which decreases the strain at failure. Temper T6 exhibits the lowest local strain at failure, whereas temper T4 shows a slightly higher local strain at failure than temper T7, which does not comply with the results for the dog-bone specimen. The strains are more confined for temper T7 (as seen from the strain fields in Fig. 1) and the local extensometer used in the notched specimens is here too large to capture the actual local strain inside the notch. The local strain inside the notch is only used to evaluate the numerical solution and its value at failure should not be interpreted as a material parameter. As also seen in Dunand and Mohr [44], two consecutive slopes of the local strain versus elongation curve are apparent regardless of the temper and notch radius, as indicated by two triangles on the curve for temper T4 in Fig. 2(a).

2.4. Single edge notched tension test

Single edge notch tension (SENT) tests were performed to investigate the influence of a sharp geometrical imperfection under simple quasi-static loading, and will be used in Section 4 to calibrate a fracture model for the finite element simulations. The geometry of the specimen and its attachment to the clamp of the test machine are shown in Fig. 3. A thin slit of 11.13 mm length was pre-cut into one of the sides, so that the tip of the slit coincides with the centre of the fastening holes. The width of the slit was measured to be between 0.35 and 0.38 mm. Any effects on the material properties from the heat that arises during wire erosion of the slits are assumed to be minimal [15]. Three of the test specimens were oriented so that the direction of the slit coincided with the rolling direction. To check for any effects from anisotropy, two more specimens with a slit orientation of 45° and 90° with respect to the rolling direction were also included, giving a total of 5 specimens for each temper.

All the SENT tests were carried out in an Instron 8800 series hydraulic universal test machine under quasi-static loading conditions. The force was measured by a 25 kN load cell attached to the actuator. The specimens were attached to the clamp of the test machine by pins and free to rotate about the attachment point. To minimize out-of-plane deflection, a 3D printed washer was placed between the specimen and the machine clamp. All tests were conducted using a constant cross-head velocity of 1.2 mm/min. A Basler acA4112-20 um camera oriented perpendicular to the specimens was used to monitor the tests with an initial frame rate of 4 Hz, which was then reduced to 1 Hz after peak force was reached. From these images, a virtual extensometer in eCorr could be used to extract displacements using 2D-DIC as previously described. No speckle pattern was painted on the surface of the specimens as this would make the crack formation harder to detect. In fact, the natural speckle on the aluminium surface was found to give good enough contrast to accurately track the displacements.

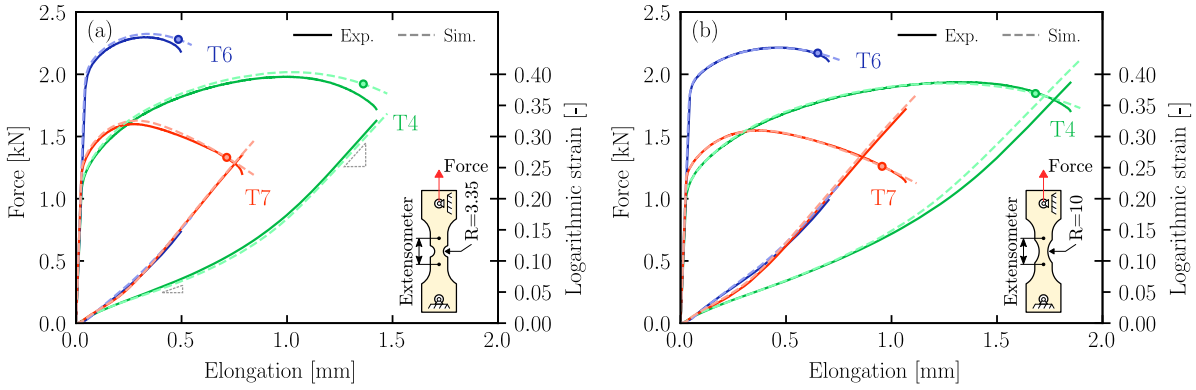

Fig. 2. Force and local logarithmic strain versus overall elongation for notched specimens with radius (a) 3.35 mm and (b) 10 mm. The elongation on the horizontal axis is found from a virtual extensometer using eCorr with an initial length of 15 mm over the notch, as shown in the figures. The logarithmic strain on the right vertical axis is calculated from a local extensometer with an initial length of 2 mm inside the notch. The different tempers are separated by the colours. The two triangles in (a) show the two consecutive slopes in the local strain seen before and after peak force. Dashed lines show predictions from simulation (discussed in Section 4), where a circle (∘) indicates the point at which the Cockcroft–Latham integral W exceeds its critical value W_c (see Eq. (4)) in the critical element. (For interpretation of the references to colour in this figure, the reader is referred to the web version of this article.)

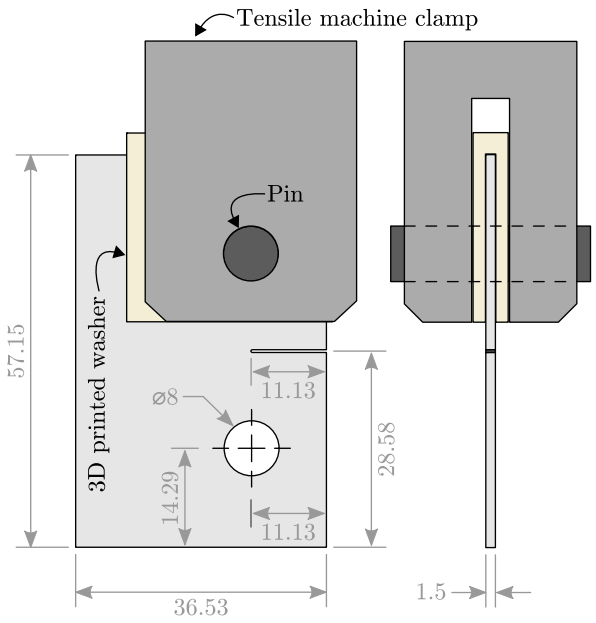

Fig. 3. Geometry and clamping of the specimen in the SENT test setup. All measures are given in mm and are the same above the notch. The specimen is attached to the clamp of the test machine by pins and thus free to rotate about the attachment point. A 3D printed washer is placed between the specimen and machine clamp to minimize out of plane deflections.

The applied force as a function of the slit opening displacement (SOD) is presented in Fig. 4. The slit opening displacement is measured from the outer corners of the slit as illustrated in the upper left figure. Tempers T4 and T7 display similar peak force at approximately 3.0 to 3.2 kN, see Fig. 4(a) and (c), respectively, whereas temper T6 shows a notably higher peak force at approximately 3.8 to 3.9 kN, see Fig. 4(b). Moreover, the slit opening displacement at peak force differs significantly between the three tempers. Temper T6 reaches peak force at the lowest slit opening displacement equal to approximately 0.6 mm, which is about half the slit opening displacement reached for temper T7 at peak force. Temper T4 has the highest slit opening displacement at peak force equal to approximately 1.5 mm. The difference in response prior to peak force is probably linked to the plasticity of the material. Temper T6 exhibits the highest 0.2% proof stress, as seen in Table 1. This allows for larger elastic deformation in the process zone in front of the slit and thus higher peak force. The lower ductility, on the other hand, initiates material failure at an earlier stage, resulting in a more rapid decline in force level subsequent to peak force. The T4 and T7 tempers display similar 0.2% proof stress. However, the hardening of the T7 temper saturates at a lower stress, which possibly results in a slightly lower peak force in the SENT tests. The tests are repeatable for specimens with a slit orientation of 0° to the rolling direction. The 45° and 90° orientations exhibit a somewhat higher peak force in all tempers. However, the differences are not substantial. It is unknown if the deviation in force for the T6 temper with an orientation of 90° (red curve in Fig. 4(b)) is due to scatter or effects from anisotropy. Some out-of-plane deflection was observed for the T4 specimen during testing. However, the amount was different between tests, suggesting that the out-of-plane deflection has only a limited effect on the response curve in Fig. 4.

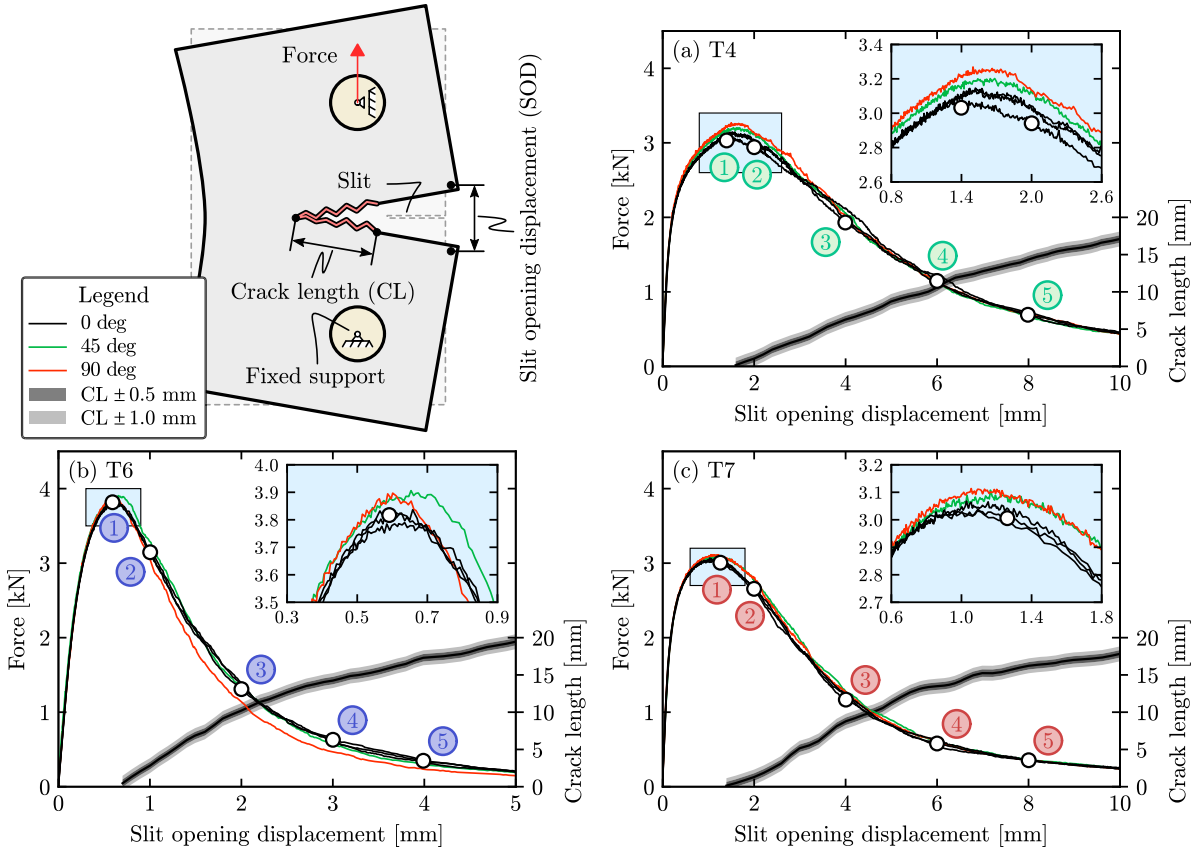

Fig. 4. Applied force and crack length (CL) as a function of the slit opening displacement (SOD) in the SENT tests. Figures (a), (b) and (c) correspond to temper T4, T6 and T7, respectively. The different orientations of the slit with respect to the rolling direction are defined by the different colours of the curves. The measured crack length is included in the lower part of the plots, with axis on the right-hand side. Confidence levels of ±0.5 mm and ±1.0 mm are included as dark and light grey shaded areas, respectively. The point marked ① defines the first point where material separation is detected on the surface of the specimens. Pictures from all marked points are given in Fig. 5. (For interpretation of the references to colour in this figure legend, the reader is referred to the web version of this article.)

Fig. 5 shows images of the specimens at the five levels of the slit opening displacement marked in Fig. 4. Image ① indicates when material separation is first detected on the outer surface of the specimens. This occurs approximately at maximum force, although fracture has probably already initiated at mid-thickness of the specimen in front of the slit where the plastic deformation is the highest. Consequently, the actual crack length is assumed to be slightly larger. Temper T6 shows the fastest crack propagation regarding the slit opening displacement, whereas temper T4 exhibits the slowest crack growth. Granum et al. [15] reported a similar observation regarding crack growth resistance for these three tempers in their study on plates subjected to pressure loads. The amount of crack growth is also reflected in Fig. 4, where the reduction of cross-section area results in a more rapid drop in force level for tempers T6 and T7 than for temper T4.

The fracture modes differ between the tempers. Morgeneyer et al. [46,47] observed the formation of orthogonal slanted strain bands that develop very early on in front of a crack tip, where final fracture occurred along one of the most prevalent bands. The result was slant fracture, i.e., the fracture surface is slanted at an angle of about ±45° to the normal direction of the plate. Both tempers T4 and T6 exhibited slant fracture, as shown in Fig. 6(a) and (b). Irregular flipping (i.e., flipping does not occur at a specific distance of crack growth) between the ±45° orientations was also seen for temper T4, cf. Fig. 5(a). In contrast, the T7 temper showed a cup-cup fracture mode, which is favoured when extensive thinning of the fracture zone occurs. This thinning is clearly visible in Fig. 6(c).

3. Low-velocity impact tests

3.1. Experimental setup

The low-velocity impact tests were carried out in an Instron CEAST 9350 drop tower with a maximum kinetic energy of 1800 J. The setup is illustrated in Fig. 7(a). Square plates with a dimension of 312.5 mm by 312.5 mm were clamped inside the impact chamber using two cylindrical steel clamping rings. The dimensions of the clamping rings and test specimens are shown in Fig. 7(b). Twelve M12 bolts were used to fasten the plate between the two clamping rings, thus preventing sliding of the plate and ensuring proper boundary conditions.

The hemispherical impactor in Fig. 7(c) has a radius of 75 mm and is mounted on an instrumented striker with a calibrated load cell located approximately 230 mm from the tip of the impactor. The load cell measures the force at discrete points in time with a sampling rate of 500,000 Hz. A total of 15,000 sampling points were taken during each test. A photocell system measured the velocity of the striker just before impact. The impactor and the attachment have a mass of 1.572 kg, while the weight of the striker below the load cell is 0.492 kg. The total mass m_2 under the load cell thus adds up to be 2.064 kg. Including 6.5 kg of additional weights, the total mass m_1 above the load cell is 11.736 kg. The total mass of the impacting system $m_p = m_1 + m_2$ equals 13.8 kg.

The velocity v and the displacement w of the impactor during impact are obtained from the following trapezoidal integration scheme [48]

$$v_{n+1} = v_n - \left(\frac{F_{n+1} + F_n}{2m_p} - g\right)\Delta t \tag{1a}$$

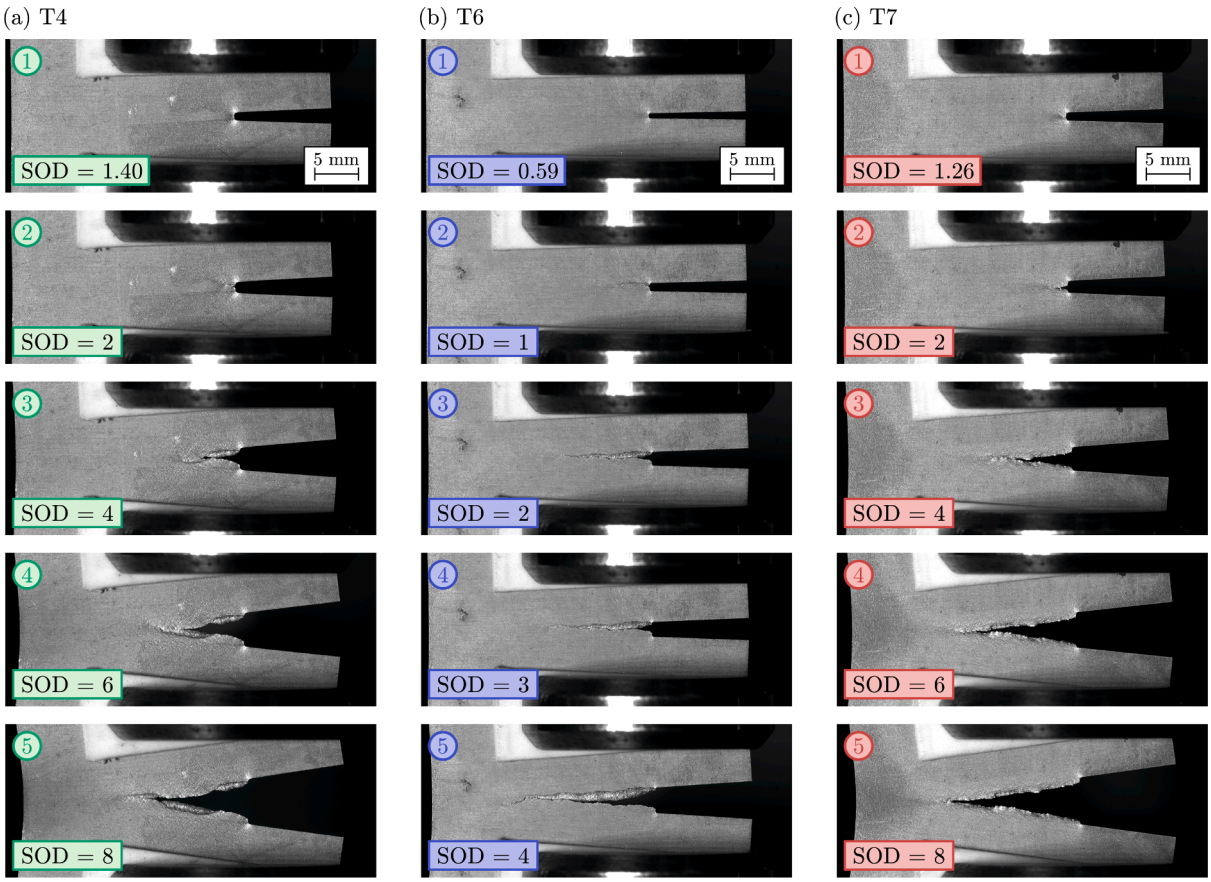

Fig. 5. Images of crack propagation in specimens in tempers (a) T4, (b) T6 and (c) T7. The pictures are taken from specimens with the slit along the rolling direction. The numbers refer to the five levels of slit opening displacement marked in Fig. 4. The first image is taken as material separation is first detected on the specimen surface. The slit opening displacement (SOD) in mm is given in all figures.

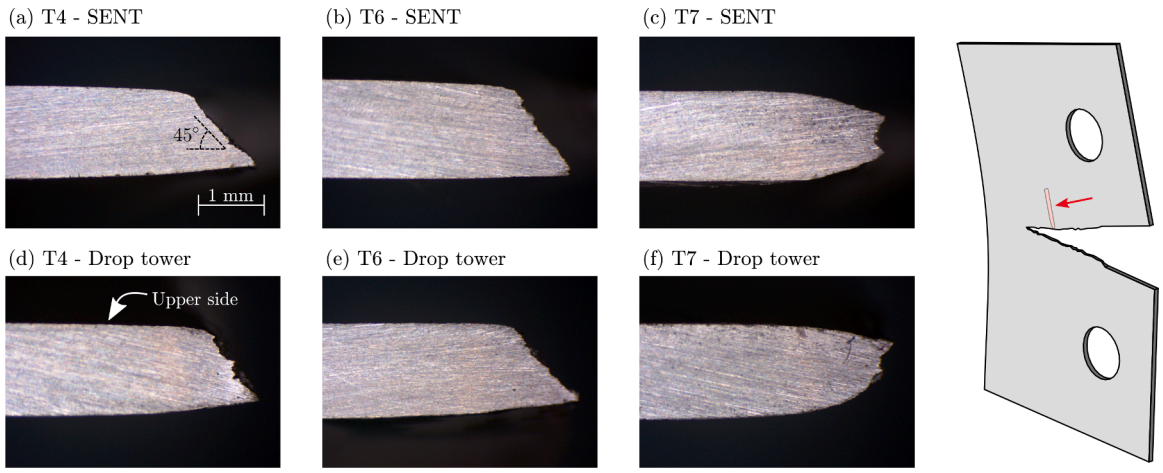

Fig. 6. Fracture zone profiles of selected (a)/(b)/(c) SENT tests and (d)/(e)/(f) drop tower tests (discussed in Section 3.3). The rightmost figure shows how the profiles are extracted from the SENT tests. The profiles from the drop tower test are extracted similarly. The ±45° angle and scale are shown in (a).

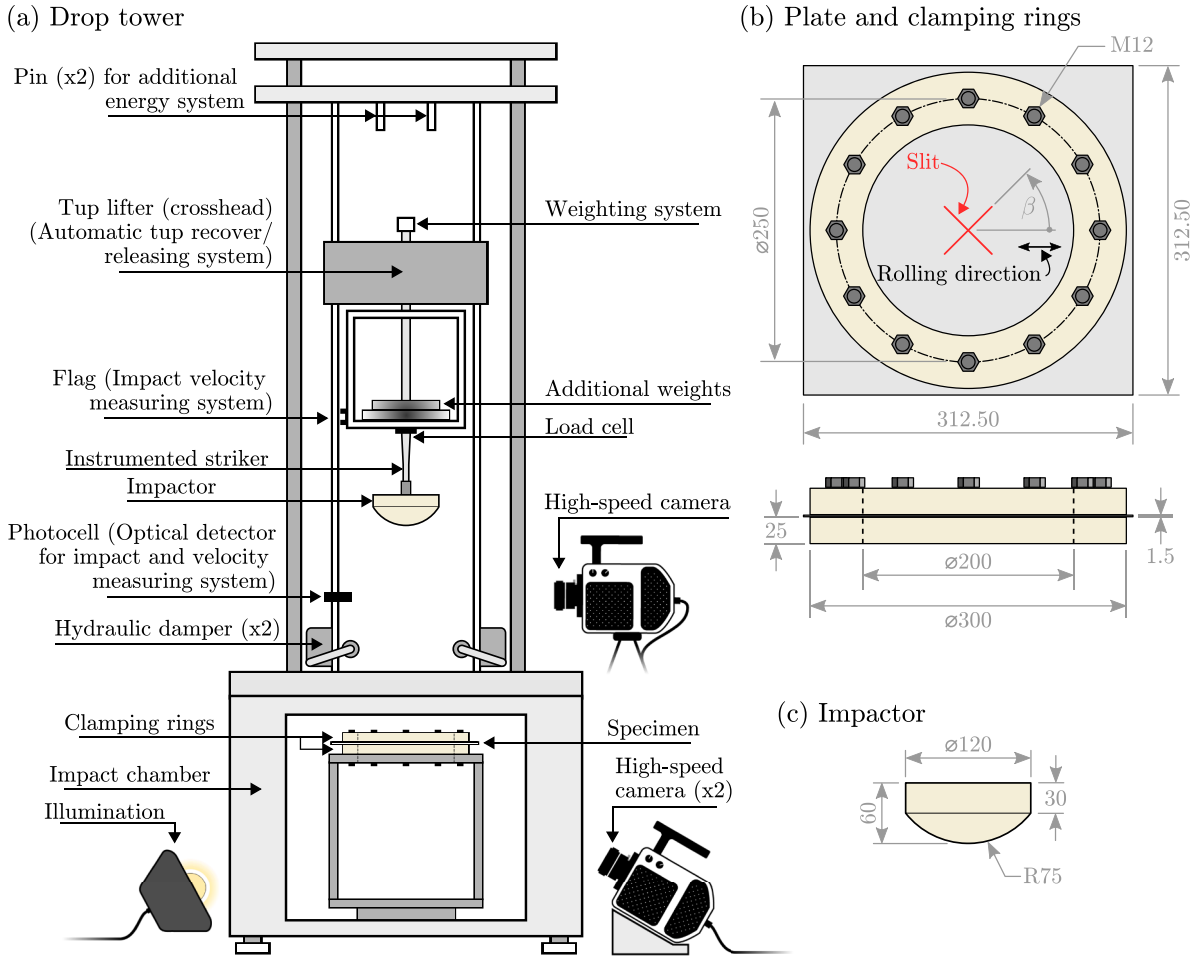

Fig. 7. Experimental setup of the impact tests: (a) drop tower, (b) geometry of the plate and clamping rings, and (c) geometry of the impactor. All measures are in mm. The orientation of the slit is given as an angle β with respect to the rolling direction, as shown in figure (b).

$$w_{n+1} = w_n + \left(\frac{v_{n+1} + v_n}{2}\right)\Delta t \tag{1b}$$

where F is the resisting force from the target plate on the impactor, $g = 9.81\ \mathrm{m/s^2}$ is the gravitational acceleration and $\Delta t = 0.002$ ms is the sampling time. The subscripts n and $n+1$ represent two subsequent values of a variable. As the load cell is not located at the tip of the impactor, we must account for the mass below the load cell to find the correct resistance force from the plate to the impactor. Dynamic equilibrium gives the resistance force F from the measured force P at the load cell as [48]

$$F = \left(1 + \frac{m_2}{m_1}\right) P \tag{2}$$

where m_1 and m_2 are the mass above and below the load cell, respectively. The ratio m_2/m_1 is approximately equal to 0.176. Thus, the resistance force is 17.6% higher than the measured force. We emphasise that the force measurements reported in this work are directly provided by the instrumented striker of the Instron drop tower rig without any additional filtering.

Two synchronised Phantom v2511 high-speed cameras with a resolution of 1280 × 800 pixels and a frame rate of 25,000 frames per second were used to monitor the deformation of the plates from below, as shown in Fig. 7(a). Using 3D-DIC, available in eCorr, the deformation profile of the plates could be measured. To verify the calculation of the displacements from the force measurements in Eq. (1), a third high-speed camera was used to monitor the position of the instrumented striker during impact. The difference between these two separate measurements of displacement was found to be approximately 0.5 to 1.0 mm for the plates without slits and approximately 0.3 to 0.8 mm for plates with slits, depending on the impact velocity. Details about this study have been excluded for brevity. As the differences are small, displacements calculated from the force measurements will be used henceforward if nothing else is said. This is advantageous as we do not have to synchronize the data and account for the small vertical translation of the drop tower, which is discussed below.

3.2. Results for plates without slits

Tests on plates without slits were performed for three different target impact velocities equal to 6, 8 and 10 m/s. The force-displacement curves from these tests are presented in Fig. 8, where it appears that the measured initial velocity was consistently slightly lower than the target value. The impactor did not perforate the plate in any of these tests, as can be seen from the rebound in the response curves, and fracture was not seen in any of the tested plates. The shape of the force-displacement curves indicates that the impact event has two stages. In the first stage, the load is carried by bending actions and the stiffness is low, whereas in the second stage, membrane actions carry the load and the stiffness is markedly higher. The oscillations in the force signals seen in Fig. 8 are directly related to elastic stress waves that propagate along in the striker. This was verified in finite element analyses where the impactor and the part of the instrumented striker in front of the additional weights were included as deformable solids, while the mass above the load cell was included as a concentrated point mass. The period of these oscillations was measured to be between 0.5 and 0.58 ms (1,700 to 2,000 Hz).

The plates in temper T6, which has the highest yield and ultimate strength of the three tempers, display the highest stiffness and peak force and the lowest maximum displacement of the impactor, see Fig. 8(b). Similar response is exhibited by the plates in tempers T4 and T7, see Fig. 8(a) and (c), respectively, except for the highest impact velocity where the T4 plate has higher stiffness and peak strength and lower maximum displacement. The dashed response curves in Fig. 8(b) are

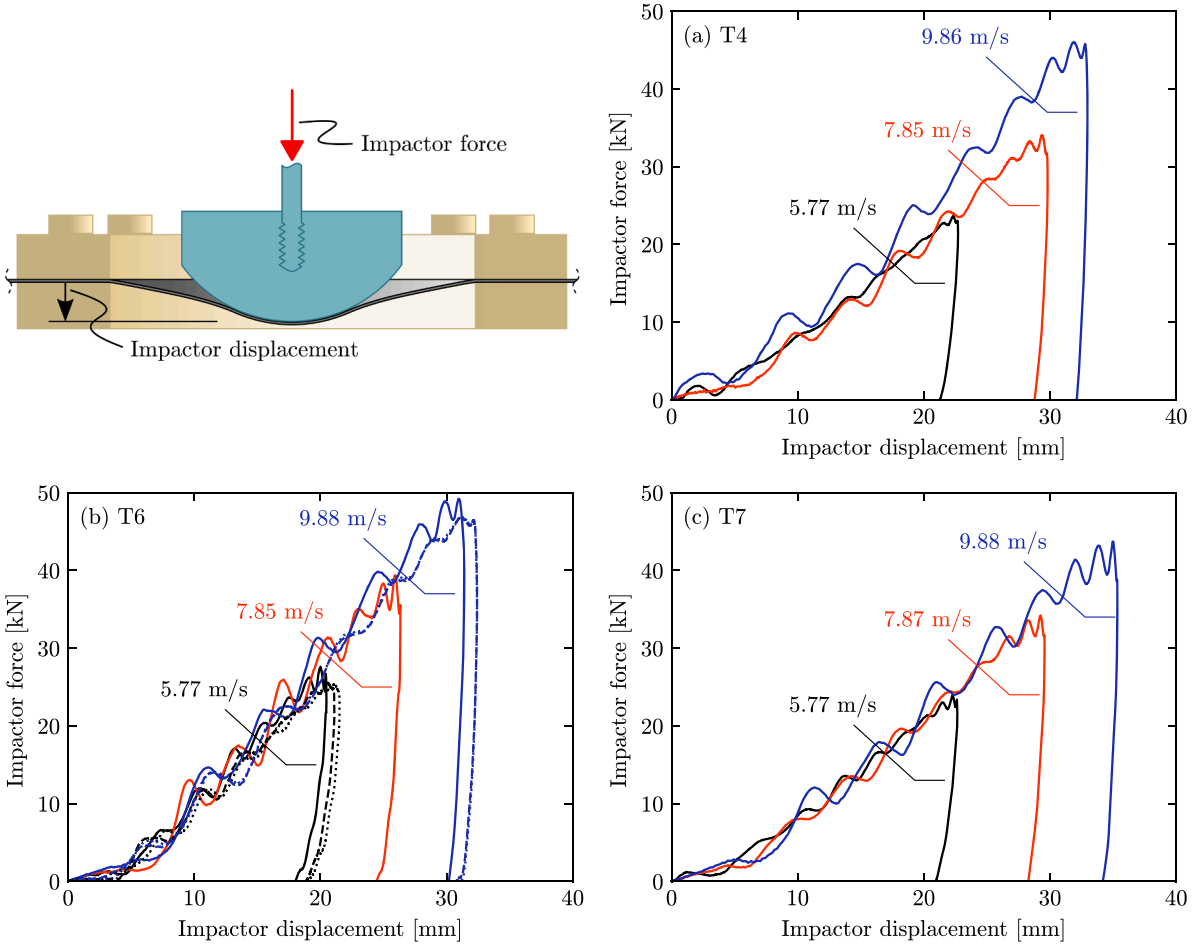

Fig. 8. Resisting force from the target plate on the impactor as a function of displacement of the tip of the impactor for temper: (a) T4, (b) T6 and (c) T7. The two measurements are defined in the upper left figure. Different colours define the measured velocity before impact. The four dashed response curves in figure (b) are from repeated tests on plates in temper T6.

repeated tests for temper T6, which show that the repeatability of the drop tower tests is satisfactory.

Fig. 9 displays the cross-section of the plates at distinct points in time (coloured curves) and at maximum displacement w_{max} (black curves), extracted from 3D-DIC analyses. Initially, all plates show the same deformed profile independent of temper. After about 3 ms, membrane actions become dominating and the displacement of the plates in temper T6 starts to deviate from that of the plates in the other two tempers. At this transition, the whole drop tower starts to translate, which can be seen in the outer left region of the deformed profile of the plates. As seen in Fig. 10, the translation of the drop tower was found to vary linearly with the peak force, where the maximum displacement was on average 2.4, 3.0 and 3.9 mm, ranging from the lowest to the highest impact velocities. As will be seen below, the presence of a slit greatly reduces the peak force, and the translation of the drop tower was less than 1 mm in all tests on plates with slits. The plates in T4 and T7 temper display a similar deformed shape at the maximum displacement.

3.3. Results for plates with slits

Tests on plates with slits were performed for three different target impact velocities: 4, 6 and 8 m/s. Fig. 11 shows the force-displacement curves from these tests. Again, the measured initial velocities given in the figure deviate somewhat from the target velocities, but stay consistent between tests. The orientation β of the slits with respect to the rolling direction, as defined in Fig. 7(b), is indicated by the line style used in the plots. Unlike for the tests of plates without slits, the peak force is only slightly increased by a higher impact velocity. However, the impact velocity influences the amount of ductile tearing, and thus the impactor displacement. Plates in temper T4 and T7 display similar force levels and maximum displacement, but the force drops somewhat faster after reaching the peak force for the plates in T4 temper. The impactor nose does not fully perforate the plate for the two lowest impact velocities, as indicated by the change in direction of the impactor. Perforation occurs only for the highest velocity. The plates in T6 temper display the lowest peak force and the highest impactor displacement, and the impactor perforates the plate at the intermediate and highest impact velocity. The reason for the low peak force is that fracture initiates while the contribution from membrane actions is negligible due to the low ductility of the T6 temper. In contrast, the specimens in temper T6 exhibited the highest peak force in the SENT test, see Fig. 4. Thus, high ductility seems to be preferable over high strength in the low-velocity impact test, but this is not a general rule valid for all plate tearing problems. The tests with the two lowest impact velocities were repeated with a slit orientation of 22.5° and 45° and the results are shown by dashed lines in Fig. 11. The effects of slit orientation are clearly inconsiderable and the limited anisotropy found in the tension tests can be neglected.

Fig. 12 shows snapshots of the plates at an impactor displacement of 10, 15 and 20 mm for a target impact velocity of 4 m/s. A picture at maximum displacement is also included for comparison. For the plate in temper T6, crack initiation occurs before an impactor displacement of 15 mm, as indicated by the scaled view in the figure. The plate deformation is similar between the three tempers at this point, which indicates that the earlier initiation for the plate in temper T6 is due to the lower ductility. Crack initiation occurs later for the plates in temper T4 and T7, which explains the higher peak force. We also find that crack initiation occurs before peak force in all tests. The deformation at maximum displacement is similar for plates in temper T4 and T7, whereas the crack has propagated further for the plate in temper T6, allowing larger displacement of the impactor. Similarly to the SENT tests in Section 2.4, the plates in temper T4 and T6 show a slant fracture mode, whereas the plates in temper T7 experience a cup-cup fracture mode. Profiles of the fracture zone are shown in Fig. 6(d), (e) and (f) for tempers T4, T6 and T7, respectively. The slant fracture flips irregularly for the plates in T4 temper and only occasionally for the plates in T6 temper.

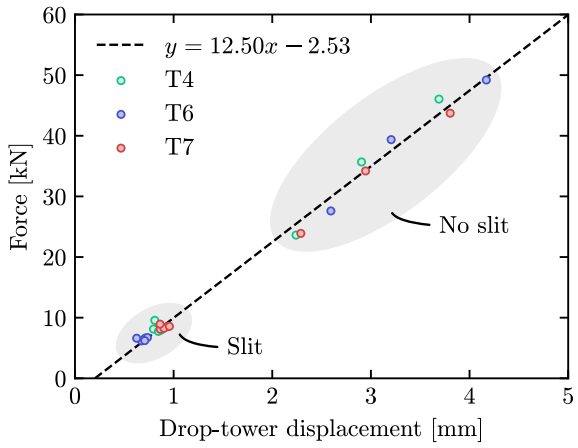

Fig. 10. Relation between maximum force exerted on the impactor and the maximum measured translation of the drop tower from 3D-DIC measurements. The colours on the markers separate the three tempers. The shaded regions collect the experiments from plates with and without slits. A trend line is included to emphasize the linear relation between the measured force and displacement of the drop tower, though the validity at a very small impactor force is questionable. (For interpretation of the references to colour in this figure legend, the reader is referred to the web version of this article.)

The possible effect of friction on the resisting force from the target on the impactor and the crack propagation was investigated in a separate test series, where both the impactor and target plate were coated with a dry Teflon (PTFE) lubricant. The tests showed that the response of the plates was not influenced by the lubrication, and it is reasonable to assume that friction has only a minor effect on the results from the low-velocity impact tests.

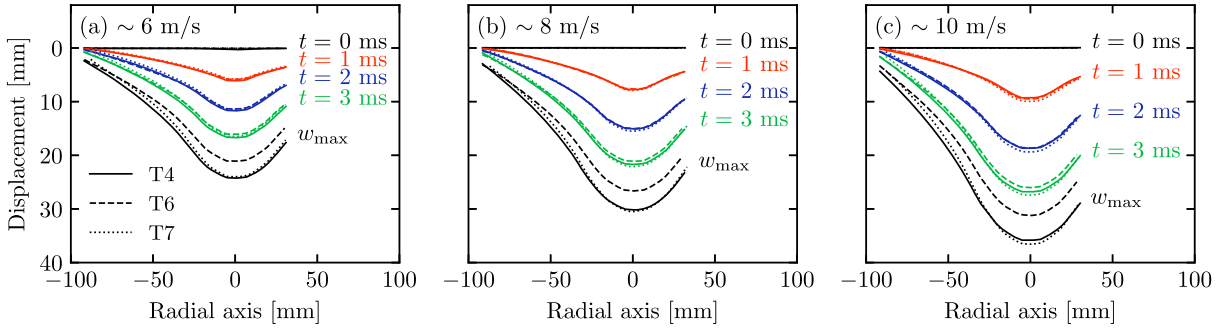

Fig. 9. Cross-section of the plates at 0, 1, 2 and 3 ms, and at the maximum displacement w_{max} for target velocity: (a) 6, (b) 8 and (c) 10 m/s. The vertical axis defines the displacement in mm. The horizontal axis defines the distance from the centre of the plate. The colour of the curves indicates the point in time, while the line type defines the temper, as shown in the legend of figure (a). Black curves show the profile at maximum displacement.

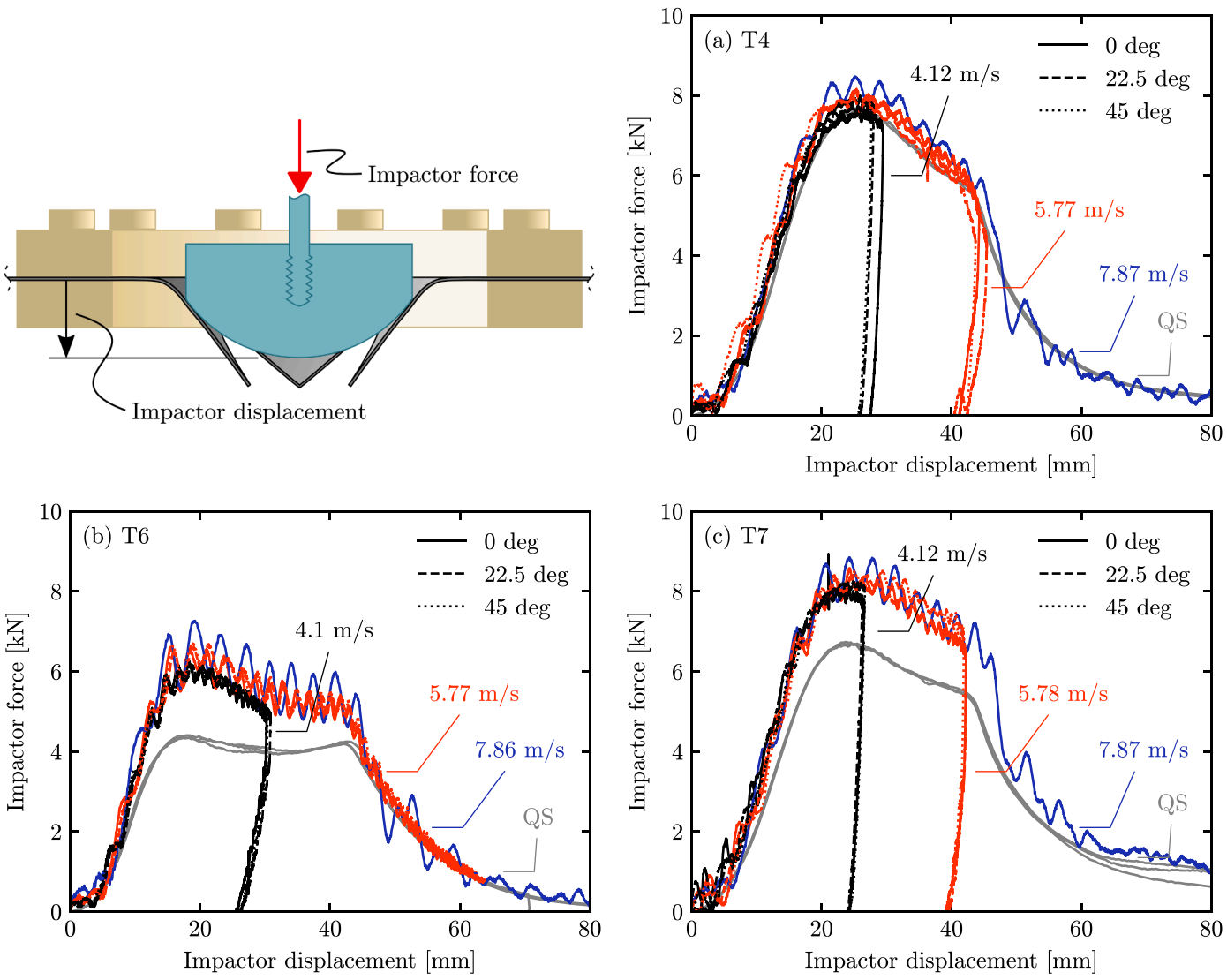

Fig. 11. Resisting force from the target on the impactor as a function of the displacement of the impactor for temper: (a) T4, (b) T6 and (c) T7. All measurements are defined in the upper left figure. Different colours define the measured initial velocity before impact. The line style defines the orientation of the slit, as given by the legends. The quasi-static response is shown by gray curves and given the label "QS".

3.4. Quasi-static tests on plates with slits

Quasi-static tests on plates with slits were performed to study the response when inertia effects are not present. The same clamping frame, specimen geometry and impactor as shown in Fig. 7 were used, but the tests were carried out in an Instron 5566 series universal testing machine with a 10 kN load cell attached to the actuator for continuous force measurements. A Basler acA2440-75 um camera was used to monitor the impactor displacement with a frame rate of 1 Hz. All quasi-static tests were conducted using a constant cross-head velocity of 12 mm/min. Three repeated tests were performed for plates with a slit orientation of 0° with respect to the rolling direction.

The quasi-static response is included in Fig. 11 as grey lines and indicated by the label "QS". While the resisting force on the impactor is reduced by approximately 27% and 15% for temper T6 and T7, respectively, almost no difference is observed between the dynamic and quasi-static response for temper T4. As will appear from the finite element simulations discussed in Section 5.3, the lower force level can be related to how resilient the plates are to crack growth. Consequently, the differences in force level are believed to be directly related to the change in material behaviour under high deformation rate, rather than being a result of inertia effects.

4. Material modelling

4.1. Constitutive equations

Finite element (FE) simulations combining von Mises plasticity with the Cockcroft–Latham fracture model [38] were employed to simulate the low-velocity impact tests. The model parameters were calibrated by means of inverse modelling using the results from the notch tension tests and the SENT tests.

A hypo-elastic plastic formulation of von Mises plasticity was adopted, which is valid for small elastic deformations but allows for large plastic deformations and large rotations. Linear hypo-elasticity was formulated in terms of the Jaumann rate of the Cauchy stress tensor and the elastic behaviour is governed by Young's modulus E and Poisson's ratio ν. Plasticity was modelled in terms of the von Mises yield criterion, the associated flow rule and isotropic hardening. The flow stress σ_f is defined by

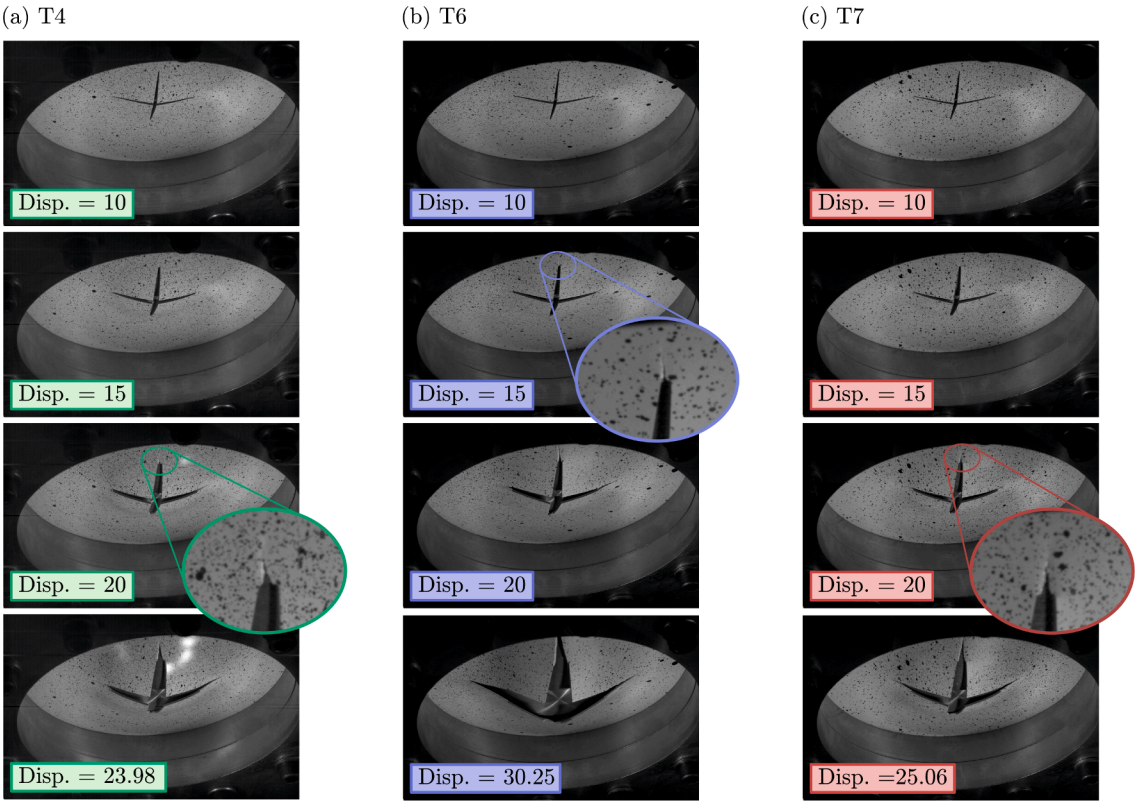

Fig. 12. Snapshots of deformed plates in temper (a) T4, (b) T6 and (c) T7 at target impact velocity 4 m/s and impactor displacement of 10, 15 and 20 mm. Pictures at maximum displacement are also included for comparison. The scaled views in the figure show the formation of cracks, but crack initiation occurs at an earlier point.

$$\sigma_{\mathrm{f}} = \sigma_0 + \sum_{i=1}^{2} Q_i \left(1 - \exp(-C_i p)\right) \tag{3}$$

where p is the equivalent plastic strain. The initial yield stress is denoted σ_0 and the isotropic hardening is controlled by the parameters Q_i and C_i, which define the saturation stress and rate of saturation, respectively, of the two terms of the hardening rule.

The Cockcroft–Latham fracture model is used to predict fracture in the simulations, and the Cockcroft–Latham integral W is defined by

$$W = \int_0^p \max(\sigma_I, 0)\mathrm{d}p \leq W_{\mathrm{c}} \tag{4}$$

where σ_I is the major principal stress. The fracture parameter W_{c} is the critical value of W at which an element is eroded, i.e., the stress in the element is set to zero. The fracture model implicitly depends on the stress triaxiality T and the Lode parameter L via the major principal stress, i.e.,

$$\sigma_I = \left(T + \frac{3 - L}{3\sqrt{3 + L^2}}\right)\sigma_{\mathrm{eq}} \tag{5}$$

The stress triaxiality T and the Lode parameter L are defined by

$$T = \frac{\sigma_{\mathrm{H}}}{\sigma_{\mathrm{eq}}}, \quad L = \frac{2\sigma_{II} - \sigma_I - \sigma_{III}}{\sigma_I - \sigma_{III}} \tag{6}$$

where σ_{eq} is the von Mises equivalent stress, σ_{H} is the hydrostatic stress, and $\sigma_I \geq \sigma_{II} \geq \sigma_{III}$ are the ordered principal stresses. By combining Eqs. (4) and (5) it appears that the Cockcroft–Latham integral W is driven by the plastic power multiplied by a factor that accounts for the influence of the stress triaxiality and the Lode parameter.

All simulations were carried out in the commercial FE-software Abaqus/Explicit [49]. The flow stress model in Eq. (3) was implemented using a VUHARD user-subroutine, whereas the fracture model in Eq. (4) was implemented using a VUSDFLD user-subroutine. We emphasise that the VUSDFLD only operates on values of the field variables at the start of the increment. However, the stable time increment in the explicit analysis is sufficiently small (between 0.9×10^{-8} and 1.3×10^{-8} s) to ensure good accuracy.

4.2. Identification of model parameters

We follow the approach in Granum et al. [37] for calibrating the plasticity parameters. A first estimate on the initial yield stress σ_0 and the hardening parameters Q_i and C_i was found by a fit to the Cauchy stress versus logarithmic plastic strain curve up to necking for the UT200 specimen in the rolling direction, shown in Fig. 1. The parameters defining the second hardening term, i.e., Q_2 and C_2, were then adjusted to obtain an optimal fit to the force-displacement curve of the NT10 specimen in Fig. 2(b) through an inverse modelling approach using the optimization tool LS-OPT [50] in combination with Abaqus/Explicit [49]. Eight-node linear brick elements with reduced integration and hourglass control (C3D8R in Abaqus) and a target element size of 0.15 mm was used, which corresponds to 10 elements over the plate thickness. Only one-eighth of the specimen was modelled, as shown in Fig. 13 (b), due to the assumed symmetry about the xy-, yz- and xz-plane. Young's modulus $E = 70,000$ MPa and Poisson's ratio $\nu = 0.3$ were adopted in all simulations to describe the elastic behaviour of aluminium. A density of 2,700 kg/m^3 was assigned to the material.

The calibrated values of the initial yield stress and the hardening parameters are compiled in Table 2 and the force-displacement curves from the simulations of the notched specimens are included as dashed lines in Fig. 2. Both the global and local responses are well represented in the simulations of the tension tests on the NT10 specimens, but a premature onset of localized necking is observed for the T4 temper. The force is somewhat overestimated in the simulation of the tension tests on the NT3 specimens, while the local strains are still well described. This

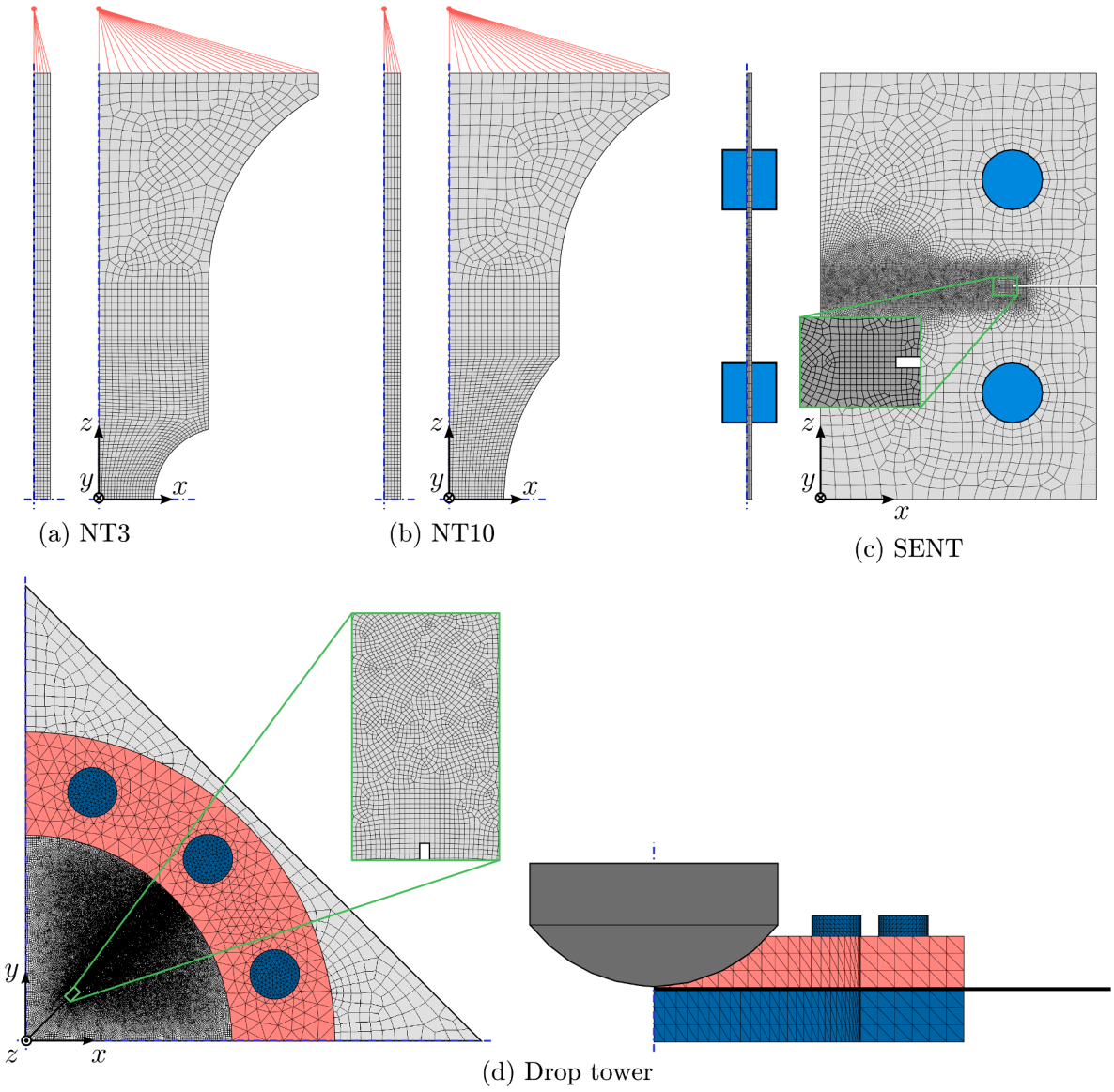

Fig. 13. Finite element models of (a) NT3, (b) NT10 and (c) SENT specimens and (d) plate with slits mounted in the drop tower. The symmetry faces are marked by blue dash-dotted lines. Red lines indicate a rigid link between constrained nodes and a reference point.

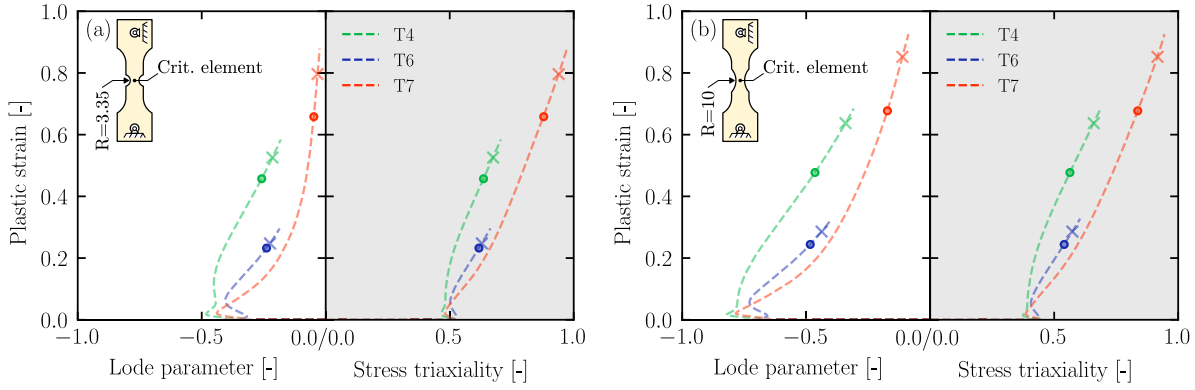

Fig. 14. Evolution of stress triaxiality and Lode parameter as a function of plastic strain in the critical element of (a) the NT3 specimen and (b) the NT10 specimen. A circle (∘) represents the point at predicted fracture in the simulation, while a cross (×) indicates the point which corresponds to the elongation at fracture for the experiments in Fig. 2. (For interpretation of the references to colour in this figure legend, the reader is referred to the web version of this article.)

Table 2
Initial yield stress, hardening and fracture parameters.

Temper	σ_0 [MPa]	Q_1 [MPa]	C_1 [−]	Q_2 [MPa]	C_2 [−]	W_c [MPa]
T4	132.06	81.19	20.82	146.28	4.60	155.0
T6	224.63	17.81	483.10	88.87	14.11	83.0
T7	145.18	3.89	5,529.28	68.77	32.18	185.0

overestimation is probably related to the use of the quadratic von Mises yield criterion in the plasticity model, which is independent of the Lode parameter. It has been found that the non-quadratic Hershey–Hosford yield criterion [51,52] gives an improved description of yielding and plastic flow of isotropic aluminium alloys, but at the cost of substantially increasing the CPU time of the simulations. Fig. 14 shows the evolution of the stress triaxiality T and the Lode parameter L with plastic strain at the centre element of both specimens, clearly indicating a stress state closer to generalized shear ($L = 0$) than generalized tension ($L = -1$) for the NT3 specimen. As shown in Granum et al. [37], a plasticity model based on the Hershey–Hosford yield criterion, which depends on the Lode parameter, would have given better agreement with the experimental data for both specimens. The stress triaxiality is slightly higher in the NT3 specimen than in the NT10 specimen, and increases significantly with the plastic strain in both cases.

The fracture parameter W_c was calibrated using the SENT test by means of a trial and error method, and the values for the three tempers are compiled in Table 2. An illustration of the FE model is shown in Fig. 13(c). The same element type as used in the previous simulations was applied. An element size of 0.15 mm was targeted in the centre of the specimen where the crack propagates and then it gradually increased away from this region. Symmetry was utilized at the mid-surface (the xz-plane) to decrease the computational cost. As a consequence, out-of-plane deflections were prohibited. An accurate representation of the slant fracture mode is also prohibited by the use of symmetry, yet slant fracture can probably not be predicted with von Mises plasticity without including heterogeneities introduced by the microstructure [46,47].

The attachment to the test machine was represented by contact boundary conditions between the pins (blue parts in Fig. 13(c)), which were modelled as analytical rigid bodies, and the specimen. The sharp notch was explicitly represented in the mesh as two neighbouring rows without elements. The orientation of the mesh plays a significant role on the predicted crack path when element erosion is used to describe fracture [15,24]. The mesh in front of the slit was made by a structured meshing technique to ensure the correct element size where the crack initiates, followed by an irregular mesh pattern that was generated using the sweep meshing technique with advancing front in Abaqus/CAE. We found that the irregular mesh gave a crack path in the simulations that was more in accordance with the experiments.

The applied force versus slit opening displacement curves are shown in Fig. 15(a) for the three tempers, where the shaded areas define the outer boundaries of the experimental data. With appropriate calibration, the Cockcroft–Latham fracture model is able to capture the experimental response. The point of crack initiation, i.e., when the first element is eroded in the centre of the specimen, occurs before peak force as indicated by the circles in the plot. Fig. 15(b) shows the crack length measured on the surface (dashed lines) and in the centre (dash-dotted lines) of the finite element model as a function of the slit opening displacement. The crack length measured on the surface of the specimens in the experiments is included in the figure as thick solid lines, where the shaded areas show a confidence level of ±0.5 mm and ±1.0 mm. The crack length on the surface of the specimen is well represented in the simulations for all tempers, but the first element in the simulation is eroded slightly before cracking is detected in the experiments. Detecting material separation in the experiments on a macroscopic scale is not completely accurate as cracks start to form on a microscopic scale. Consequently, it is expected that there will be a slight difference in crack length between the observation in the experiments and the simulation as element erosion is a very distinct event. Moreover, crack length in the centre is generally ahead of the experimental value. The reason for the latter observation is that the higher stress triaxiality in the centre leads to the crack tunnelling effect, i.e., the crack propagates somewhat faster in the centre than at the surface of the specimen. Consequently, there is a clear mismatch between when cracking is first observed in the experiments (marked by ① in Fig. 4) and when the first element is eroded in the simulation as indicated in Fig. 15 as “initiation”.

By assuming quasi-static, proportional loading, the fracture surface $p_f = p_f(T,L)$, associated with the Cockcroft–Latham fracture model was constructed. The result is shown in Fig. 16 as fracture loci $p_f = p_f(T)$ for three values of the Lode parameter that represent generalized tension ($L = -1$), generalized shear ($L = 0$), and generalized compression ($L = 1$). The case of plane stress is included as a dashed line, with the vertical line at $T = 1/\sqrt{3}$ defining the point of plane strain tension. It appears from the figure that the fracture strain decreases with increasing stress triaxiality for a constant value of the Lode parameter. The highest and lowest fracture strains for a given stress triaxiality are obtained for generalized compression and generalized tension, respectively, whereas generalized shear displays a slight increase in the fracture strain compared to generalized tension. Temper T7 has the highest value of the fracture parameter W_c and displays the most ductile behaviour, followed by temper T4 and T6.

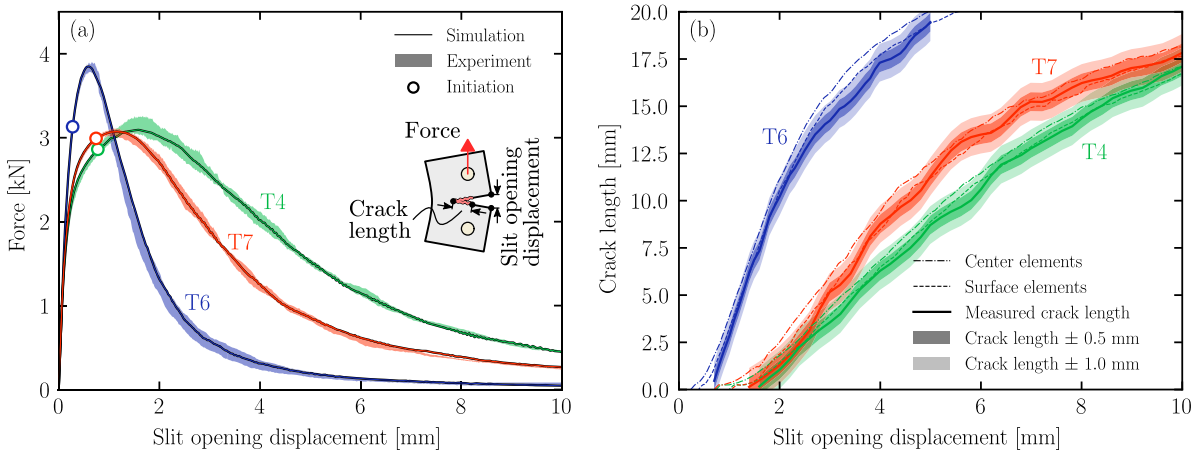

Fig. 15. Predicted (a) force and (b) crack length as a function of the slit opening displacement for the three tempers in the SENT tests. The shaded areas in (a) show the response from all experiments. The circles (◦) shows the point when the first element is eroded. The measured crack length in (b), shown by solid lines, is accompanied by a ±0.5 mm and a ±1.0 mm confidence level, shown as shaded areas.

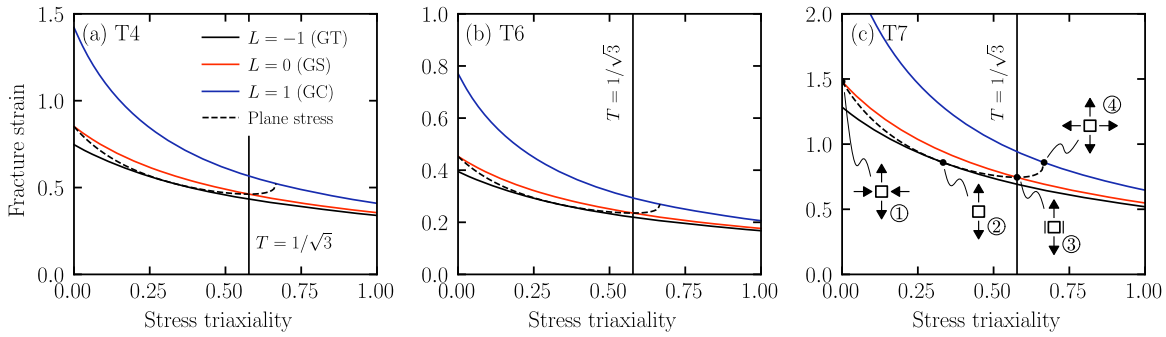

Fig. 16. Fracture loci associated with the Cockcroft–Latham fracture model giving the fracture strain p_f as a function of the stress triaxiality T for three values of the Lode parameter L. The state of plane stress is included as a dashed line. Four important stress states are indicated in (c): ① pure shear, ② uniaxial tension, ③ plane strain tension and ④ equi-biaxial tension. (For interpretation of the references to colour in this figure legend, the reader is referred to the web version of this article.)

The fracture parameter W_c of the Cockcroft–Latham fracture model was also calibrated by Granum et al. [15] for the same AA6016 alloy in tempers T4, T6 and T7 for an element size of approximately 0.5 mm. Compared to the values in Table 2, W_c for temper T7 was practically the same in their study. However, they reported a 17% higher value of W_c for temper T4 and a 87% higher value of W_c for temper T6. The substantial difference in W_c for temper T6 is most likely related to the calibration procedure. Granum et al. [15] used a flat dog-bone specimen to estimate W_c by inverse modelling. It has been seen in these types of specimens that the plastic strain, and thus the Cockcroft–Latham integral W, tend to grow rapidly in the critical element once the strain localizes, making W_c highly sensitive to the fracture strain and how well the simulation can capture the necking behaviour. We have in this paper calculated W_c from the global response of the SENT test and not the localized behaviour of a single element. We emphasize that an increase of 87% for W_c would yield poor results in the simulation of the SENT test of temper T6.

5. Simulation of low-velocity impact tests

5.1. Numerical model

Simulations of the low-velocity impact tests were performed in Abaqus/Explicit [49] using the user-subroutines described in Section 4.1. The finite element model is shown in Fig. 13(d). Only one-quarter of the plate was modelled by applying symmetry boundary conditions about the xz- and yz-plane to reduce the computational time. The top and bottom clamping rings, marked by a red and blue colour in the figure, were modelled using linear tetrahedral elements (C3D4 in Abaqus) with the elastic material properties of steel, i.e., Young's modulus $E = 210,000$ MPa and Poisson's ratios $\nu = 0.3$. The bolts were included as a part of the bottom clamping ring. Constant pressure was applied on the top clamping ring to represent the effect from the pre-tensioning of the bolts.

The impactor was modelled as an analytical rigid body with a mass of 3.45 kg, which is a quarter of the total mass of the impacting body due to the use of symmetry. The striker and additional weights were not explicitly modelled, but their masses were included as a part of the rigid body. By assuming that the mass is located at a single point within the rigid body, we avoid oscillations in the measured signals that arise when elastic stress waves propagate in the instrumented striker. The impactor is restricted from any movement other than in the striking direction and is given an initial velocity according to the impact velocity measured in the experiments.

The element mesh of the plate with slits is shown in Fig. 13(d). A total of 10 linear hexahedral elements with reduced integration and hourglass control (C3D8R in Abaqus) were used over the thickness. The target element size in the region where the crack is expected to propagate was 0.15 mm and increased gradually to 1 mm near the symmetry lines. The element size was further increased in the area outside of the clamping rings to a maximum size of 8 mm. By increasing the element size in these regions, the computational time was more than halved compared to a model with better aspect ratios on the elements, while obtaining the same response. As for the SENT specimen, a sweep meshing technique with an advancing front algorithm was used to generate an irregular mesh in the region of crack propagation, making the crack path less regular and thus more in accordance with experimental observations. The slit was represented in the mesh by two neighbouring rows with no elements. The elements in front of the slit take the form of regular cubes to avoid bad aspect ratios and distortions of elements near the slit, as shown by the zoomed-in view in Fig. 13(d). The quarter model consists of $1,361,168$ nodes in total. For the plates without slits, where fracture was not observed in the tests, the target element size was 1 mm in the impacting area with 10 elements over the thickness. The total number of nodes in this model is $171,694$.

General contact with a tangential friction coefficient of 0.1 was used between all parts in the finite element model. We will discuss the influence of friction later. The total simulation time was 10 ms for plates without slits, and between 15 and 22 ms for plates with slits, depending on the temper and impact velocity. The resisting force from the target plate on the impactor was calculated by multiplying the acceleration of the rigid impactor by four times its mass (13.8 kg) to account for the use of symmetry.

5.2. Plates without slits

As fracture did not occur in the experiments on the plates without slits, the attention is directed towards the plastic behaviour. The resisting force from the target plate on the impactor as a function of the displacement of the impactor is shown in Fig. 17 for all combinations of temper and impact velocity. The experimental results are given by dashed lines, whereas the predictions from the simulations are shown by solid lines. Different colours are used to distinguish the impact velocity. The peak force is overestimated in all simulations, and the rebound occurs more abruptly than in the experiments. We believe that the abrupt rebound in the simulations is linked to the mass of the impactor being located in a singular point. The force in the simulations is then calculated from the mass and acceleration of this point. The predicted response is in excellent agreement for the plates in temper T6, whereas the impactor displacement is overestimated with between 0.6 to 1.4 mm for the plates in temper T7. Similarly, the impactor displacement is overestimated for the plates in temper T4 with approximately 1.4 and 2.4 mm for the highest and lowest impact velocity, respectively, while showing excellent agreements for the intermediate impact velocity.

The cross-section of the plate along the radial axis at three distinct points in time is shown in Fig. 18 for the intermediate impact velocity. The deformed profile at maximum deformation w_{max} is also included in the figure. We emphasize that the deformed profiles from the experiments, shown by dashed lines, are extracted from 3D-DIC

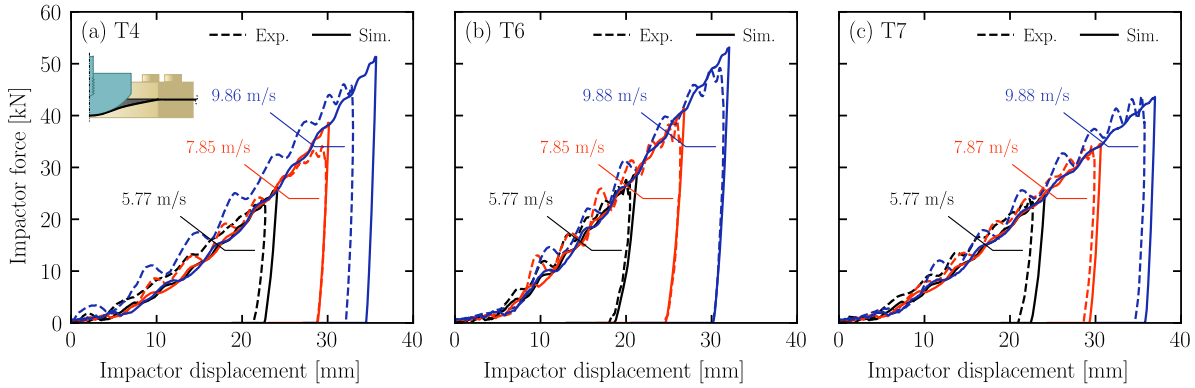

Fig. 17. Resisting force from the target plate on the impactor as a function of displacement of the tip of the impactor for temper (a) T4, (b) T6 and (c) T7. Solid and dashed lines correspond to results from simulation and experiments, respectively. Different colours define the measured velocity before impact.

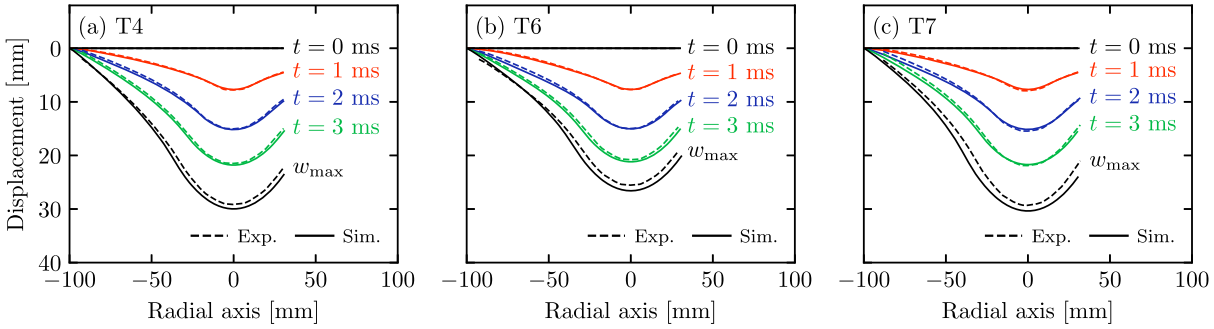

Fig. 18. Cross-sections of the plates without slits at time 0, 1, 2 and 3 ms, as well as the maximum displacement w_{max} for an impact velocity of 8 m/s (red curves in Fig. 17). Solid and dashed lines corresponds to results from simulations and experiments, respectively.

measurements. The displacements have been corrected for the translation of the drop tower previously discussed. The simulations agree well with the experiments up to $t = 3$ ms, while the maximum deformation is slightly overestimated with approximately 1 mm in the centre of the plate. The shape of the deformed profile is well represented in all cases, and we conclude that the numerical model describes the plastic deformation of the plates without slits with good accuracy.

5.3. Plates with slits

It appears that a proper representation of material failure is important to accurately capture the response of the plates with slits. Fig. 19 shows the resisting force from the target plate on the impactor as a function of the displacement of the impactor for all combinations of temper and impact velocity. The experimental results are given by dashed lines, whereas the predictions from the simulations are shown by solid lines. The colours signify the impact velocity as indicated by the labels in the figure.

With the Cockcroft–Latham fracture model calibrated from the SENT tests, the simulations of the plates in temper T4 show an almost perfect agreement with the experimental data. In contrast, the peak force is underestimated for the plates in temper T6 and T7 by approximately 1.1 and 1.0 kN, respectively. As the energy absorption in the plate, which is represented by the area enclosed by the force-displacement curves in Fig. 19, is equal to the change in the kinetic energy of the impacting mass, a lower peak force will result in a larger displacement, and

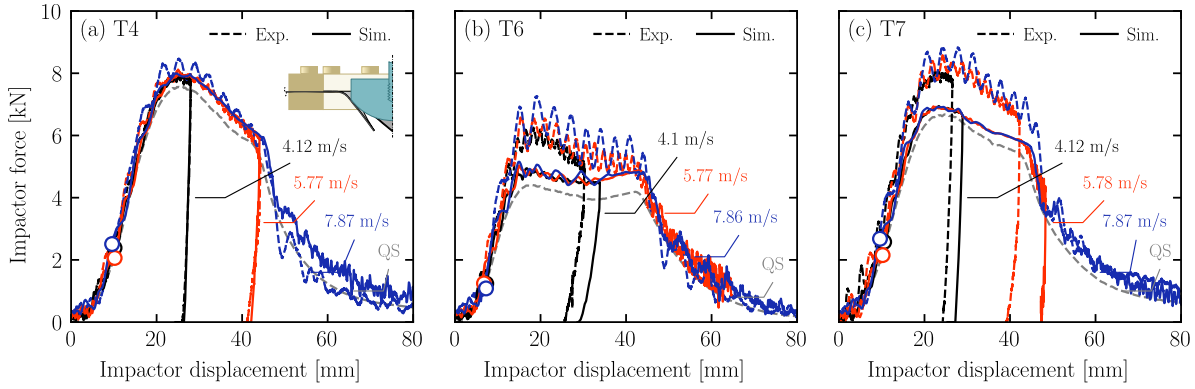

Fig. 19. Resisting force from the target plate on the impactor as a function of displacement of the tip of the impactor for temper (a) T4, (b) T6 and (c) T7. Solid and dashed lines correspond to results from simulations and experiments, respectively. Circles (∘) shows the point when the first element is eroded. The colours define the measured velocity before impact. The quasi-static response is included as gray curves. (For interpretation of the references to colour in this figure, the reader is referred to the web version of this article.)

accordingly the simulations overestimate the displacement of the impactor. All simulations capture the initial linear increase in the force and the impactor displacement at which the force drops, which represents the point where the crack has propagated far enough for the plate to lose its load-carrying capacity, i.e., perforation of the plate. This event is only linked to the structure as it occurs at the same impactor displacement for all three tempers. While the shape of the force-displacement curve is well described in the simulations of temper T7, larger discrepancies can be recognized for the T6 temper where a flat plateau at peak force is seen in the simulations. The point at which the first element is eroded from the model is indicated by a circle in Fig. 19. Crack initiation in the simulations occurs much earlier than peak force. In comparison, the peak force occurs shortly after cracking in the simulations of the SENT test, see Fig. 15.

The quasi-static response of the plates is included as grey curves in Fig. 19. Clearly, the numerical simulations of the low-velocity impact tests show a better resemblance with the force-displacement history from the quasi-static tests. Although the force is higher in the simulations, which might be related to inertia effects or strain rate sensitivity of the flow stress, the difference compared to experimental data stays rather consistent between the three tempers.

Fig. 20 compares deformed shapes of the plates in the simulations and experiments at distinct points in time for temper T4 and T6 at the lowest impact velocity. Excellent agreement is found for temper T4, whereas for temper T6 the crack grows faster in the simulation, resulting in a larger displacement of the impactor. Similar results as for temper T6 are also seen for temper T7. From these observations, it is reasonable to assume that the discrepancy in force level for plates in tempers T6 and T7 also arises from excessive crack growth in the numerical model.

5.4. Stress state along crack path

We will in the following discuss the stress state that occurs in the elements along the crack path in the SENT and low-velocity impact tests. Fig. 21 shows how the Lode parameter and stress triaxiality evolve with the equivalent plastic strain in the simulations of these tests. Only the elements in the row closest to the mid-plane of the plate are included in the figures. Material points closest to the tip of the slit are given a black colour, and the colour gradually changes to red for elements further away from the slit. Material points located further away than 15 mm from the slit are not included for the SENT specimen in Fig. 21(a)–(c). Video animations of these plots can be found in the Supplementary data available online.

The stress triaxiality is similar in both the SENT and low-velocity impact test. Material points that are close to the slit experience a slightly higher stress triaxiality than material points further away, where the stress triaxiality is slightly higher than $T = 1/\sqrt{3}$. For temper T4 and T6, the stress triaxiality starts to increase once the plastic strain is approximately half of its maximum value at failure, marking the point at which local necking occurs. This point is not as prominent for temper T7, where an increase in stress triaxiality is seen almost at the start of plastic deformation.

The evolution of the Lode parameter with respect to the plastic strain is somewhat different between the simulated SENT and low-velocity impact tests. For the SENT specimen, the Lode parameter in a given material point starts in a state between generalized shear ($L = 0$) and generalized compression ($L = 1$) before rapidly changing to a state of generalized tension ($L = -1$) as the crack approaches the considered material point. Apart from some few material points in the vicinity of the tip of the slit, the material points closer to the slit experience a higher value of the Lode parameter. The value of the Lode parameter is typically higher in the simulation of the low-velocity impact tests, initially reaching generalized compression before saturating at, or close to, generalized shear. Eventually, the Lode parameter drops towards generalized tension as the crack approaches the material point and local necking occurs. Assuming a state of plane stress prior to local necking, the stress state as function of plastic strain is initially close to equi-biaxial tension ($L = 1$ and $T = 2/3$) and then progresses towards plane-strain tension ($L = 0$ and $T = 1/\sqrt{3}$), see Fig. 16. Once local necking occurs, the stress state is no longer plane and changes towards

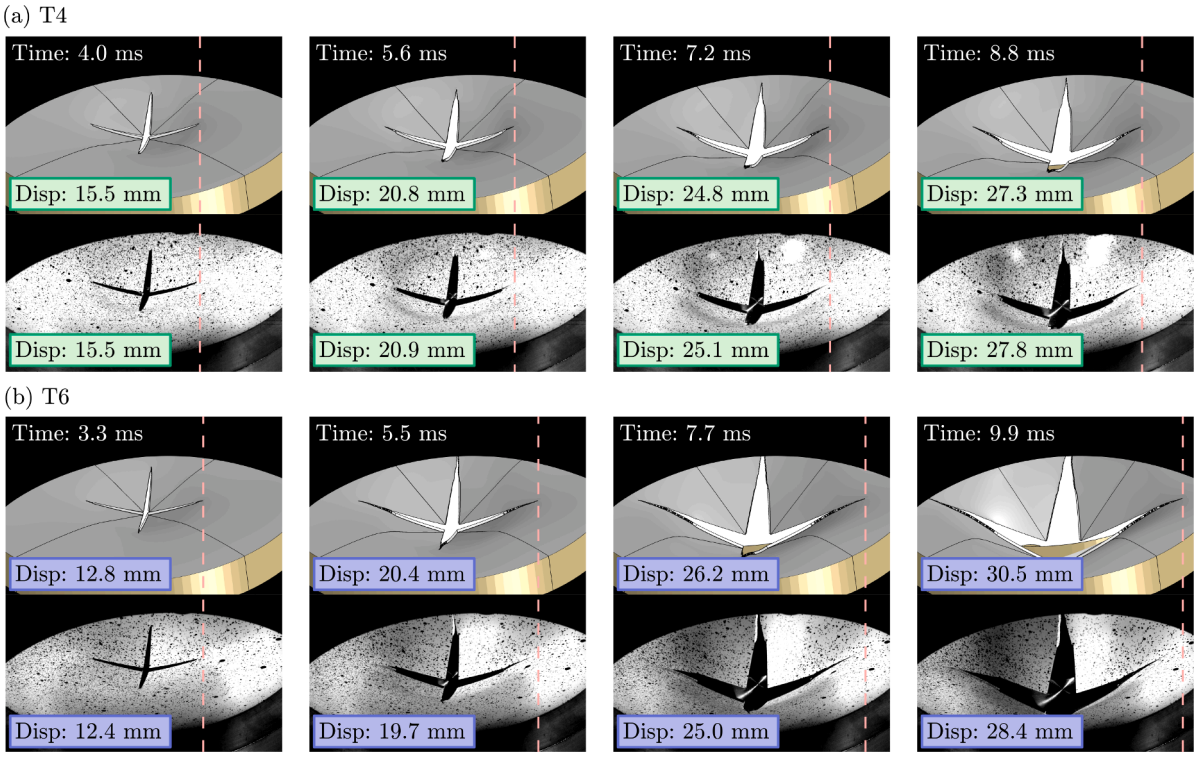

Fig. 20. Snapshots of the simulation (upper row) and experiment (lower row) for the lowest velocity at different points in time for temper (a) T4 and (b) T6. The displacement of the impactor is included in the left corners. The red lines show the position of the crack tip in the simulations.

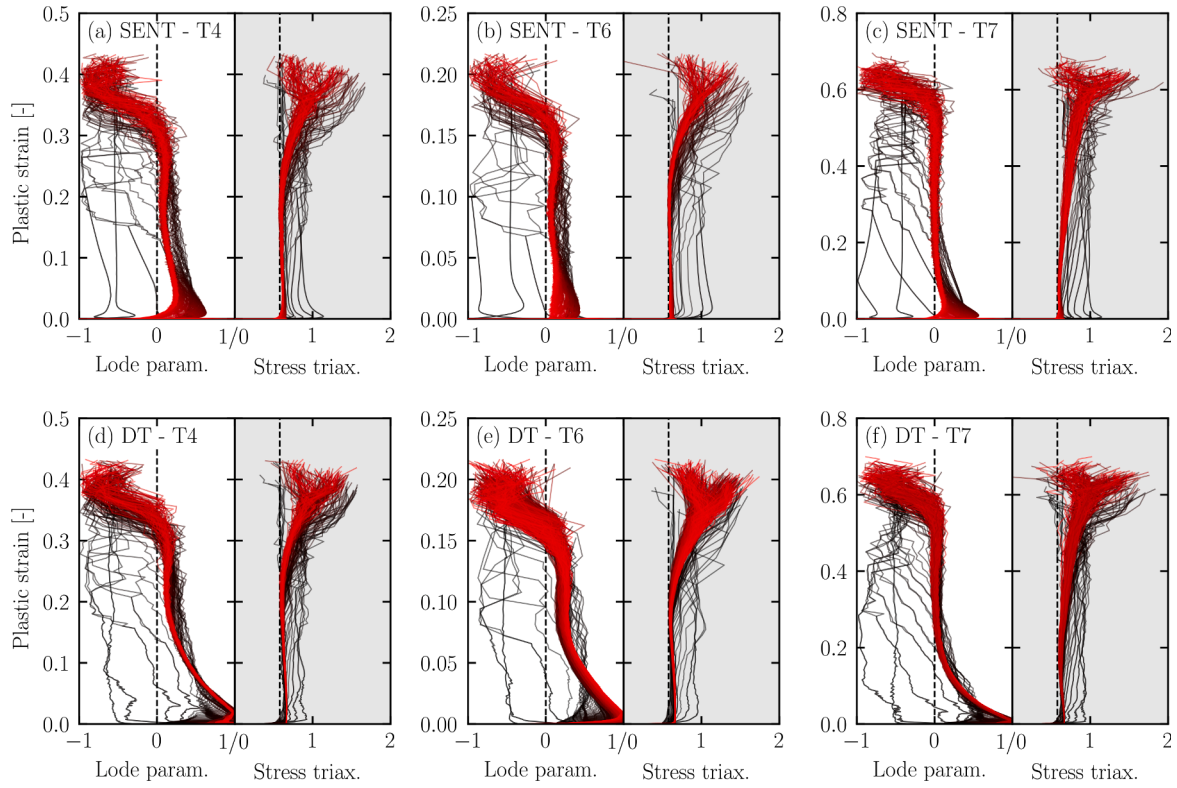

Fig. 21. Evolution of the Lode parameter and the stress triaxiality as function of plastic strain for elements that are eroded in the centre element layer in the simulation of the (a)/(b)/(c) SENT and (d)/(e)/(f) drop tower (DT) tests. Vertical dashed lines corresponds to a triaxiality of $T = 1/\sqrt{3}$ and a Lode parameter of $L = 0$ (plane strain tension). Only material points within a crack length of 15 mm are included for the SENT tests. Video animations of these plots can be found in the Supplementary data available online. (For interpretation of the references to colour in this figure, the reader is referred to the web version of this article.)

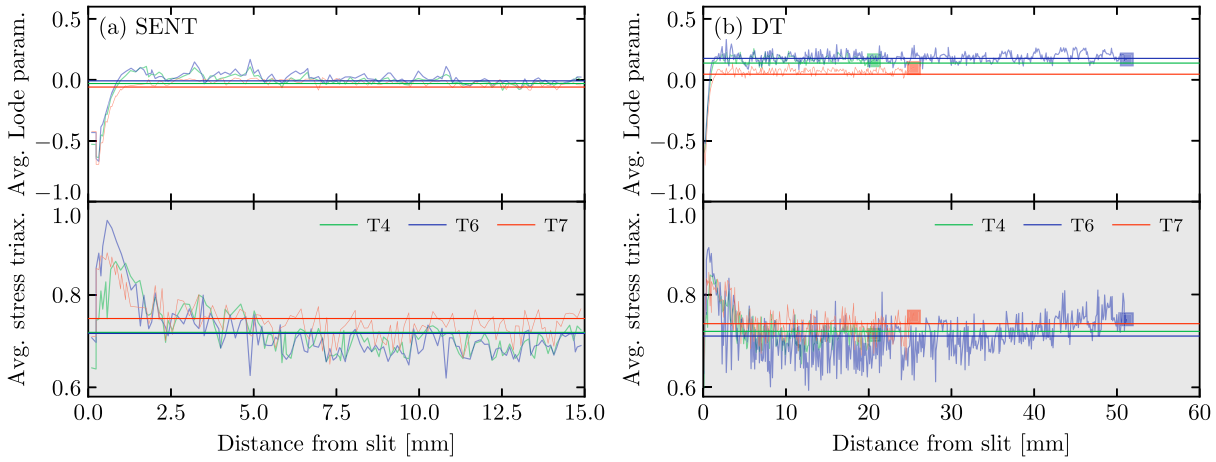

Fig. 22. Average values of the Lode parameter and stress triaxiality for the centre elements along the crack in simulations of (a) the SENT and (b) drop tower (DT) tests. The colour of the curves defines the different tempers. The horizontal lines define the average value for all material points. (For interpretation of the references to colour in this figure legend, the reader is referred to the web version of this article.)

generalized tension.

Fig. 22 shows the average values of the stress triaxiality and the Lode parameter in material points at a given distance from the slit along the crack path, defined as

$$T_{\text{avg}} = \frac{1}{p_{\text{f}}} \int_0^{p_{\text{f}}} T(p)\mathrm{d}p, \qquad L_{\text{avg}} = \frac{1}{p_{\text{f}}} \int_0^{p_{\text{f}}} L(p)\mathrm{d}p \tag{7}$$

where p_{f} is the plastic strain when failure occurs in the material point. The results for different tempers are separated by colours and defined in the legend. Horizontal lines show the mean value for all material points.

The average value of the Lode parameter near the slit is approximately -0.6, and saturates towards generalized shear ($L = 0$) about 1 mm from the slit. A marginally higher value of the Lode parameter is observed in the simulation of the drop tower test than in the corresponding simulation of the SENT test. The average values of the stress triaxiality in the simulations of the SENT and drop tower tests are similar. A low value is observed in the vicinity of the tip of the slit, followed by a rapid increase to a peak value and a subsequent slow decrease to T_{avg} between 0.70 and 0.75. The plate in temper T7 displays the highest average stress triaxiality, followed by the plates in temper T4 and T6, which exhibit similar

levels of T_{avg}.

From the simulations it appears that the stress states along the propagating crack in the SENT and drop tower tests are similar, but the value of the Lode parameter is, in general, slightly higher in the simulation of the drop tower tests. Based on localization analyses, Granum et al. [37] found that the AA6016 alloy experiences the lowest failure strain for stress states near generalized shear. The same observation was reported by Gorji and Mohr [53] in an experimental programme on AA6016 plates in temper T4 subjected to shear fracture during deep drawing. This is not in accordance with the Cockcroft–Latham fracture model, where Fig. 16 clearly shows a minimum in failure strain for generalized tension. The estimated force level in the simulation of the drop tower tests for temper T6 and T7 could be slightly improved by using a more complex failure model which explicitly accounts for the effects of the Lode parameter, but it would not eliminate the discrepancy. However, a more complex failure model would correct for the early prediction of failure observed in the simulation of the notched tension test when using the current calibration of the Cockcroft–Latham fracture model, as shown in Fig. 2.

5.5. Parametric study

A parametric study has been conducted to check how sensitive the plate response is to the assumptions made in the simulations presented in Section 5.3. Fig. 23 shows how the peak impactor force deviates from the experiment for the different factors shown on the horizontal axes and in Table 3. It was found that a good representation of the peak force also yields excellent agreements of the force-displacement response curve and crack growth in the simulation.

Friction coefficient between the plate and the impactor was set to 0.1 in the base model, which is lower than values for steel-aluminium interaction found in the literature. The difference in peak force in simulations with different friction coefficients is shown in Fig. 23 by orange bars. Changes in friction coefficient influence the results from the simulations, where a higher coefficient results in an increase in peak force. In fact, the peak force was found to increase linearly within the narrow range of friction coefficients investigated. Temper T6 was found to be least influenced by the friction coefficient, followed by temper T7 and T4. Consequently, the magnitude of the resisting force from the target plate on the impactor seems to be the main contributing factor and not the actual distance of sliding. As previously stated, the measured force in the experiments was not noticeable influenced when the plate and impactor were coated with dry silicon-based lubricant, which also suggests that the influence from friction is already small. Assuming that the friction coefficient is the same for all tempers, these results do not explain why the force level is underestimated for tempers T6 and T7 but not for temper T4.

Effects from strain rate sensitivity of the flow stress are shown by red bars in Fig. 23. We refer to Granum et al. [15] for the constitutive relation used that includes both strain rate sensitivity and thermal softening effects. Only a minor increase in peak force is obtained for temper T4 and T6, whereas for temper T7 a moderate increase is displayed when $c = 0.005$. Chen et al. [54] reported a strain-rate sensitivity parameter c between 0.0015 and 0.0038 for alloy AA6060 and AA6082 in temper T6. In that study, $\dot{p}_0 = 0.001\text{s}^{-1}$ was used, while we have used $\dot{p}_0 = 0.0005\ \text{s}^{-1}$. Low strain-rate sensitivity at room temperature was also reported by Vilamosa et al. [55] for the same aluminium alloys. These findings suggest that the effects of the strain rate sensitivity of the flow stress are not significant.

By including effects from thermal softening due to adiabatic heating, the peak force is slightly reduced. The reduction is more notable for temper T7 where the increase in temperature due to adiabatic heating was 45–55 °C in the eroded elements. The change in temperature for temper T4 and T6 was 27–47 °C and 10–25 °C, respectively, and the reduction in peak force is consequently less notable. This observation is in accordance with Rakvåg et al. [17] who observed no change in the predicted response of pressure loaded plates with preformed holes when accounting for thermal softening. We emphasize that they did not observe any failure of the plates in their study.

The purple bars in Fig. 23 show how changes in the fracture model affect the peak force. Increasing the fracture parameter W_c by 25% (value 1 in the figure) has a pronounced effect on temper T4 and T6, whereas temper T7 shows only a modest change in peak force due to the more localized necking. We emphasize that an increase in 25% would yield unsatisfactory results in the simulation of the SENT test in Fig. 15. As seen from the response curves in Fig. 24, the fracture parameter W_c must be increased by approximately 25% for temper T6 and 60% for temper T7 in order to capture the low-velocity impact behaviour accurately. The peak strain rate in the elements along the crack in the finite element simulations was found to be in the range of $1{,}000\text{s}^{-1}$, and the strain rate increases rapidly once the crack approaches the considered material point. Based on the calibration in Roth and Mohr [56], the equivalent plastic strain at fracture was increased by approximately 35% and 90% for DP590 and TRIP780 steels, respectively, when increasing the strain rate from 0.001s^{-1} to $1{,}000\text{s}^{-1}$. Based on these observations, the underestimation of the resisting force discussed in Section 5.3 could

Table 3
Complimentary values to Fig. 23.

	Base model	Value 1	Value 2
Friction coefficient	0.1	0.0	0.3
Rate sensitivity[a]	$c = 0.0$	$c = 0.001$	$c = 0.005$
Thermal softening[a]	Not included	Included	
Fracture model	CL	CL with $1.25{\cdot}W_c$	MMC[b]

[a] See Table 5 in Granum et al. [15] for other material constants.
[b] Modified Mohr–Coulomb fracture model calibrated in Granum et al. [37].

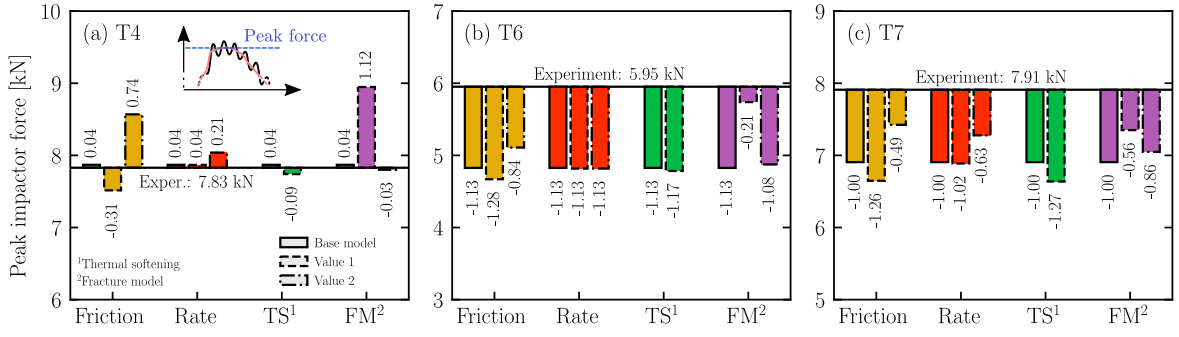

Fig. 23. Difference in peak resisting force from the target plate on the impactor for different factors in the parametric study. Peak force from experiments is shown as a horizontal line, whereas the bars show the deviation from the experiment. Peak force is measured as the maximum force after a running average filter has been applied to the response curves, as indicated in figure (a). Different values are separated by the style of the border lines, and summarized in Table 3. Different parameters are separated by colours. (For interpretation of the references to colour in this figure, the reader is referred to the web version of this article.)

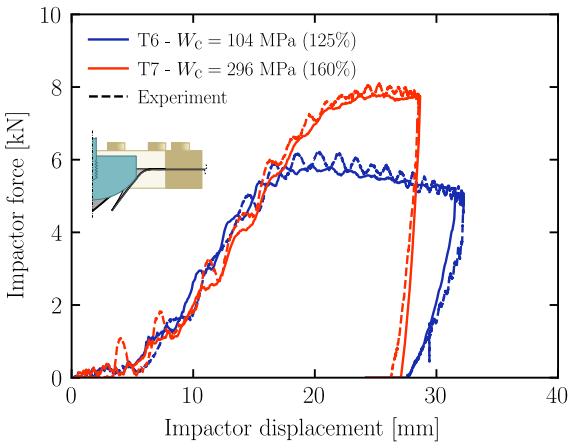

Fig. 24. Simulated resisting force from the target plate on the impactor as a function of displacement of the tip of the impactor when the fracture parameter W_c is increased with 25% for temper T6 (blue curve) and 60% for temper T7 (red curve). Dashed curves in the same colours show the result from the test in the drop tower. Only results for an impact velocity of 4.1 m/s are compared. (For interpretation of the references to colour in this figure legend, the reader is referred to the web version of this article.)

be caused by a strain rate dependence of the fracture strain that is not captured by the Cockcroft–Latham fracture model. However, if this is the explanation, the strain rate dependence of the fracture strain would have to differ substantially between various tempers of the same alloy.

The modified Mohr–Coulomb fracture model (value 2 in Fig. 23), calibrated by the use of localization analysis in Granum et al. [37] for the same materials, gives essentially the same results as the Cockcroft–Latham fracture model calibrated in Section 4.2 both in simulations of the low-velocity impact tests and the quasi-static SENT tests (not shown here for brevity). The calibration of the modified Mohr–Coulomb fracture model is completely independent from the identification method applied here, which indicates that the Cockcroft–Latham fracture model is already properly calibrated for ductile tearing under quasi-static conditions.

6. Concluding remarks

The main findings from this study are summarized as follows:

- The amount of crack growth for a given deformation of the SENT specimen and the low-velocity impact specimen is highest for temper T6, which has the lowest ductility. Moreover, temper T6 displays the highest peak force for the SENT specimen and the lowest peak force for the low-velocity impact specimen of the three tempers. Thus, it is not sufficient to only consider strength against ductility in the design of structures prone to ductile tearing. The geometry and load case must also be taken into consideration.
- Intact plates with high strength are more resilient to deformation in the low-velocity impact tests. When geometrical defects in the form of pre-cut slits are introduced, high ductility is preferable in this type of test. The response of the plates seems unaffected by the orientation of the slit, suggesting that the modest anisotropy seen in tension tests does not influence the ductile tearing of the material.
- When the loading is changed from (dynamic) low-velocity impact to quasi-static push-through, a significant reduction in peak force is observed for plates with pre-cut slits in temper T6 and T7. Only a minor reduction in peak force is observed for temper T4. There are clear indications that this change in peak force is mostly related to the behaviour of the material under high strain rates while the inertia effects are minor.
- The Cockcroft–Latham fracture model is applied to describe crack initiation and propagation in the finite element simulations. While the response is accurately captured in the SENT test, to which the fracture model is calibrated, the finite element simulations of the low-velocity impact tests underestimate the peak force and overestimate the deformation for plates with pre-cut slits in temper T6 and T7. In contrast, excellent agreement is obtained for plates in temper T4. The discrepancy between the simulations and experiments is related to the resilience to crack growth in the plates, and the parametric study shows that good agreement can be achieved by increasing the fracture parameter W_c of the Cockcroft–Latham fracture model by a significant amount. Moreover, the peak force obtained in the dynamic simulations is similar to the peak force in the quasi-static push-through tests for all three tempers. Thus, a strain rate dependence of the fracture parameter W_c might be necessary to capture the experimental results, but only for tempers T6 and T7. Further experimental studies which isolate the effects of strain rate on fracture are recommended.
- The simulations of the quasi-static SENT test and low-velocity impact tests show a similar stress triaxiality history in the material points along the crack path for a given temper, while there is a slight difference in the deviatoric stress state, as represented by the Lode parameter. Plates in temper T7 display a somewhat higher stress triaxiality than plates in tempers T4 and T6, which is probably related to the development of a more profound local neck in the former plates. The stress state is initially plane, which during plastic deformation changes from a state of biaxial tension to a state close to plane strain tension. As the crack tip approaches a given material point along the crack path, the stress state starts to deviate from plane stress conditions. At this point, the stress triaxiality increases gradually, while the stress state becomes close to generalized tension.

CRediT authorship contribution statement

Vetle Espeseth: Conceptualization, Methodology, Software, Formal analysis, Investigation, Writing – original draft, Visualization. **Tore Børvik:** Conceptualization, Methodology, Writing – review & editing, Supervision. **Odd Sture Hopperstad:** Conceptualization, Methodology, Writing – review & editing, Supervision.

Declaration of Competing Interest

The authors declare that they have no known competing financial interests or personal relationships that could have appeared to influence the work reported in this paper.

Acknowledgements

The authors gratefully appreciate the financial support from NTNU and the Research Council of Norway through the FRINATEK Program, Project no. 250553 (FractAl). The authors would like to acknowledge Ms. Jasmine Canali from the Polytechnic University of Milan (Politecnico di Milano) and Mr. Trond Auestad for assisting with the experimental programme.

Supplementary material

Supplementary material associated with this article can be found, in the online version, at doi:10.1016/j.ijimpeng.2022.104261

References

[1] Corbett GG, Reid SR, Johnson W. Impact loading of plates and shells by free-flying projectiles: a review. Int J Impact Eng 1996;18(2):141–230. https://doi.org/10.1016/0734-743X(95)00023-4.

[2] Langseth M, Larsen PK. Dropped objects' plugging capacity of steel plates: an experimental investigation. Int J Impact Eng 1990;9(3):289–316. https://doi.org/10.1016/0734-743X(90)90004-F.

[3] Langseth M, Larsen PK. The behaviour of square steel plates subjected to a circular blunt ended load. Int J Impact Eng 1992;12(4):617–38. https://doi.org/10.1016/0734-743X(92)90271-T.

[4] Langseth M, Larsen PK. Dropped objects' plugging capacity of aluminium alloy plates. Int J Impact Eng 1994;15(3):225–41. https://doi.org/10.1016/S0734-743X(05)80015-6.

[5] Wen HM, Jones N. Experimental investigation into the dynamic plastic response and perforation of a clamped circular plate struck transversely by a mass. Proc Inst Mech Eng, Part C 1994;208(2):113–37. https://doi.org/10.1243/PIME_PROC_1994_208_107_02.

[6] Wen HM, Jones N. Low-velocity perforation of punch-impact-loaded metal plates. J Press Vessel Technol 1996;118(2):181–7. https://doi.org/10.1115/1.2842178.

[7] Langseth M, Hopperstad OS, Berstad T. Impact loading of plates: validation of numerical simulations by testing. Int J Offshore Polar Eng 1999;9(01).https://onepetro.org/IJOPE/article/27152/Impact-Loading-of-Plates-Validation-of-Numerical

[8] Grytten F, Fagerholt E, Auestad T, Førre B, Børvik T. Out-of-plane deformation measurements of an aluminium plate during quasi-static perforation using structured light and close-range photogrammetry. Int J Solids Struct 2007;44(17):5752–73. https://doi.org/10.1016/j.ijsolstr.2007.01.026.

[9] Grytten F, Børvik T, Hopperstad OS, Langseth M. Low velocity perforation of AA5083-h116 aluminium plates. Int J Impact Eng 2009;36(4):597–610. https://doi.org/10.1016/j.ijimpeng.2008.09.002.

[10] Fagerholt E, Grytten F, Gihleengen BE, Langseth M, Børvik T. Continuous out-of-plane deformation measurements of AA5083-h116 plates subjected to low-velocity impact loading. Int J Mech Sci 2010;52(5):689–705. https://doi.org/10.1016/j.ijmecsci.2009.11.013.Special Issue in Honor of Professor Tongxi Yu

[11] Holmen JK, Hopperstad OS, Børvik T. Low-velocity impact on multi-layered dual-phase steel plates. Int J Impact Eng 2015;78:161–77. https://doi.org/10.1016/j.ijimpeng.2014.12.005.

[12] Gruben G, Langseth M, Fagerholt E, Hopperstad OS. Low-velocity impact on high-strength steel sheets: an experimental and numerical study. Int J Impact Eng 2016;88:153–71. https://doi.org/10.1016/j.ijimpeng.2015.10.001.

[13] Aune V, Valsamos G, Casadei F, Langseth M, Børvik T. On the dynamic response of blast-loaded steel plates with and without pre-formed holes. Int J Impact Eng 2017;108:27–46. https://doi.org/10.1016/j.ijimpeng.2017.04.001.

[14] Elveli BS, Iddberg MB, Børvik T, Aune V. On the strength–ductility trade-off in thin blast-loaded steel plates with and without initial defects—An experimental study. Thin-Walled Struct 2022;171:108787. https://doi.org/10.1016/j.tws.2021.108787.

[15] Granum H, Aune V, Børvik T, Hopperstad OS. Effect of heat-treatment on the structural response of blast-loaded aluminium plates with pre-cut slits. Int J Impact Eng 2019;132(May):103306. https://doi.org/10.1016/j.ijimpeng.2019.05.020.

[16] Li Y, Wu W, Zhu H, Wu Z, Du Z. The influence of different pre-formed holes on the dynamic response of square plates under air-blast loading. Eng Fail Anal 2017;78:122–33. https://doi.org/10.1016/j.engfailanal.2017.03.002.

[17] Rakvåg KG, Underwood NJ, Schleyer GK, Børvik T, Hopperstad OS. Transient pressure loading of clamped metallic plates with pre-formed holes. Int J Impact Eng 2013;53:44–55. https://doi.org/10.1016/j.ijimpeng.2012.07.013.

[18] Aune V, Valsamos G, Casadei F, Langseth M, Børvik T. Fluid-structure interaction effects during the dynamic response of clamped thin steel plates exposed to blast loading. Int J Mech Sci 2021;195:106263. https://doi.org/10.1016/j.ijmecsci.2020.106263.

[19] Benzerga AA, Leblond JB. Ductile fracture by void growth to coalescence. Adv Appl Mech 2010;44:169–305. https://doi.org/10.1016/S0065-2156(10)44003-X.

[20] Knott JF. Fundamentals of fracture mechanics. London: Butterworths; 1973.

[21] Li W, Siegmund T. An analysis of crack growth in thin-sheet metal via a cohesive zone model. Eng Fract Mech 2002;69(18):2073–93. https://doi.org/10.1016/S0013-7944(02)00013-9.

[22] Pardoen T, Hachez F, Marchioni B, Blyth PH, Atkins AG. Mode I fracture of sheet metal. J Mech Phys Solids 2004;52(2):423–52. https://doi.org/10.1016/S0022-5096(03)00087-5.

[23] El-Naaman SA, Nielsen KL. Observations on mode I ductile tearing in sheet metals. Eur J Mech - A/Solids 2013;42:54–62. https://doi.org/10.1016/j.euromechsol.2013.04.007.

[24] Simonsen BC, Törnqvist R. Experimental and numerical modelling of ductile crack propagation in large-scale shell structures. Mar struct 2004;17(1):1–27. https://doi.org/10.1016/j.marstruc.2004.03.004.

[25] Felter CL, Nielsen KL. Assisted crack tip flipping under mode I thin sheet tearing. Eur J Mech - A/Solids 2017;64:58–68. https://doi.org/10.1016/j.euromechsol.2017.01.009.

[26] Nielsen KL, Gundlach C. Crack tip flipping under mode I tearing: investigated by X-ray tomography. Int J Solids Struct 2017;118–119:119–27. https://doi.org/10.1016/j.ijsolstr.2017.04.014.

[27] Nielsen KL, Felter CL. Parameter window for assisted crack tip flipping: studied by a shear extended Gurson model. Int J Solids Struct 2019;171:135–45. https://doi.org/10.1016/j.ijsolstr.2019.04.021.

[28] McClintock FA. A criterion for ductile fracture by the growth of holes. J Appl Mech 1968;35(2):363–71. https://doi.org/10.1115/1.3601204.

[29] Rice JR, Tracey DM. On the ductile enlargement of voids in triaxial stress fields. J Mech Phys Solids 1969;17(3):201–17. https://doi.org/10.1016/0022-5096(69)90033-7.

[30] Barsoum I, Faleskog J. Rupture mechanisms in combined tension and shear-experiments. Int J Solids Struct 2007;44:1768–86. https://doi.org/10.1016/j.ijsolstr.2006.09.031.

[31] Gao X, Zhang T, Hayden M, Roe C. Effects of the stress state on plasticity and ductile failure of an aluminum 5083 alloy. Int J Plast 2009;25(12):2366–82. https://doi.org/10.1016/j.ijplas.2009.03.006.

[32] Wierzbicki T, Bao Y, Lee YW, Bai Y. Calibration and evaluation of seven fracture models. Int J Mech Sci 2005;47:719–43. https://doi.org/10.1016/j.ijmecsci.2005.03.003.

[33] Gruben G, Hopperstad OS, Børvik T. Evaluation of uncoupled ductile fracture criteria for the dual-phase steel Docol 600DL. Int J Mech Sci 2012;62(1):133–46. https://doi.org/10.1016/j.ijmecsci.2012.06.009.

[34] Li H, Fu MW, Lu J, Yang H. Ductile fracture: experiments and computations. Int J Plast 2011;27(2):147–80. https://doi.org/10.1016/j.ijplas.2010.04.001.

[35] Lian J, Wierzbicki T, Zhu J, Li W. Prediction of shear crack formation of lithium-ion batteries under rod indentation: comparison of seven failure criteria. Eng Fract Mech 2019;217(April):106520. https://doi.org/10.1016/j.engfracmech.2019.106520.

[36] Morin D, Hopperstad OS, Benallal A. On the description of ductile fracture in metals by the strain localization theory. Int J Fract 2018;209(1). https://doi.org/10.1007/s10704-017-0236-9.

[37] Granum H, Morin D, Børvik T, Hopperstad OS. Calibration of the modified Mohr–Coulomb fracture model by use of localization analyses for three tempers of an AA6016 aluminium alloy. Int J Mech Sci 2021;192(June 2020):106122. https://doi.org/10.1016/j.ijmecsci.2020.106122.

[38] Cockcroft M.G., Latham D.J.. Ductility and the workability of metals; vol. 96. 1968.

[39] Dey S, Børvik T, Hopperstad OS, Leinum JR, Langseth M. The effect of target strength on the perforation of steel plates using three different projectile nose shapes. Int J Impact Eng 2004;30(8):1005–38. https://doi.org/10.1016/j.ijimpeng.2004.06.004.Eighth International Symposium on Plasticity and Impact Mechanics (IMPLAST 2003)

[40] Kane A, Børvik T, Berstad T, Benallal A, Hopperstad OS. Failure criteria with unilateral conditions for simulation of plate perforation. Eur J Mech - A/Solids 2011;30(4):468–76. https://doi.org/10.1016/j.euromechsol.2011.02.003.

[41] Costas M, Morin D, Sønstabø JK, Langseth M. On the effect of pilot holes on the mechanical behaviour of flow-drill screw joints. Experimental tests and mesoscale numerical simulations. J Mater Process Technol 2021;294(February). https://doi.org/10.1016/j.jmatprotec.2021.117133.

[42] Fagerholt, E., 2017. eCorr v4.0 documentation. http://folk.ntnu.no/egilf/ecorr/doc/.

[43] Qvale K, Hopperstad OS, Reiso O, Tundal UH, Marioara CD, Børvik T. An experimental study on pre-stretched double-chamber 6000-series aluminium profiles subjected to quasi-static and dynamic axial crushing. Thin-Walled Struct 2021;158(May 2020). https://doi.org/10.1016/j.tws.2020.107160.

[44] Dunand M, Mohr D. Hybrid experimental-numerical analysis of basic ductile fracture experiments for sheet metals. Int J Solids Struct 2010;47(9):1130–43. https://doi.org/10.1016/j.ijsolstr.2009.12.011.

[45] Mohr D, Marcadet SJ. Micromechanically-motivated phenomenological Hosford–Coulomb model for predicting ductile fracture initiation at low stress triaxialities. Int J Solids Struct 2015;67–68:40–55. https://doi.org/10.1016/j.ijsolstr.2015.02.024.

[46] Morgeneyer TF, Khadyko M, Buljac A, Helfen L, Hild F, Benallal A, et al. On crystallographic aspects of heterogeneous plastic flow during ductile tearing: 3D measurements and crystal plasticity simulations for AA7075-t651. Int J Plast 2021;144:103028. https://doi.org/10.1016/j.ijplas.2021.103028.

[47] Morgeneyer TF, Taillandier-Thomas T, Helfen L, Baumbach T, Sinclair I, Roux S, et al. In situ 3-D observation of early strain localization during failure of thin Al alloy (2198) sheet. Acta Mater 2014;69:78–91. https://doi.org/10.1016/j.actamat.2014.01.033.

[48] Holmen JK, Olovsson L, Børvik T. Discrete modeling of low-velocity penetration in sand. Comput Geotech 2017;86:21–32. https://doi.org/10.1016/j.compgeo.2016.12.021.

[49] Abaqus/Explicit. User's Manual Version 2019. Dassault Systèmes Simulia Corp; 2019.

[50] LS OPT. User's Manual Version 5.2.1. Livermore Software Technology Corporation; 2016.

[51] Hershey AV. The plasticity of an isotropic aggregate of anisotropic face centered cubic crystals. J Appl Mech 1954;21(3):241–9.https://www.scopus.com/record/display.uri?eid=2-s2.0-0001150783&origin=inward

[52] Hosford WF. A generalized isotropic yield criterion. J Appl Mech 1972;39(2):607–9. https://doi.org/10.1115/1.3422732.

[53] Gorji MB, Mohr D. Predicting shear fracture of aluminum 6016-T4 during deep drawing: combining Yld-2000 plasticity with Hosford–Coulomb fracture model. Int J Mech Sci 2018;137:105–20. https://doi.org/10.1016/j.ijmecsci.2018.01.008.

[54] Chen Y, Clausen AH, Hopperstad OS, Langseth M. Stress-strain behaviour of aluminium alloys at a wide range of strain rates. Int J Solids Struct 2009;46(21):3825–35. https://doi.org/10.1016/j.ijsolstr.2009.07.013.

[55] Vilamosa V, Clausen AH, Børvik T, Skjervold SR, Hopperstad OS. Behaviour of Al-Mg-Si alloys at a wide range of temperatures and strain rates. Int J Impact Eng 2015;86:223–39. https://doi.org/10.1016/j.ijimpeng.2015.08.008.

[56] Roth CC, Mohr D. Effect of strain rate on ductile fracture initiation in advanced high strength steel sheets: experiments and modeling. Int J Plast 2014;56:19–44. https://doi.org/10.1016/j.ijplas.2014.01.003.